UNIVERSITÀ DEGLI STUDI DI PADOVA

Dipartimento di Fisica e Astronomia “Galileo Galilei”

Master Degree in Astrophysics and Cosmology

Final Dissertation

New Experimental Studies on Carbon Burning at LUNA

Thesis supervisor

Prof. Antonio Caciolli

Candidate

Lewis Ballard

Academic Year 2025/26

Abstract

Thesis Title

The $^{12}C+^{12}C$ fusion reaction occurs in high mass stars as well as during explosive nucleosythesis such as the ignition of a supernova type Ia on the surface of a white dwarf. This reaction is thus quite important astrophysically, however it remains not well understood at the occurring energies due to a very low cross section. To reduce uncertainty, the LUNA experiment under the Gran Sasso massif took data down to 2.1 MeV in the center of mass frame. The mountain combined with passive shielding of the detector setup allows a significant reduction in the amount of background radiation for gamma detection.

From this campaign, data was taken from radioactive sources and the $^{14}N(p,\gamma)$ reaction for the purpose of efficiency calibration. This data we used to fit an efficiency function to normalize the $^{12}C+^{12}C$ detection counts. With this, we then calculate the preliminary infinite yields for each run and compare with the previous results of Spillane et al. and Tumino et al. S*-Factors. We find that the data more closely follows that of Tumino et al., with a higher trend to the infinite yields, with significant uncertainty still.

Contents

Chapter 1

Introduction

1.1 Astrophysical Motivation

Nuclear reactions are an important factor determining the life of a star, giving the outward force to counter-balance the collapsing force of gravity. When a star is born, it begins fusion of hydrogen into helium in its core, ceasing the pre-stellar contraction. This fusion can occur in a 'p-p chain' fusing hydrogen into helium directly, or through the 'CNO cycle' using existing carbon, nitrogen, and oxygen in the core as catalysts for more efficient reactions [1].

When hydrogen fuel in the core is exhausted, the star must shift equilibrium to begin burning helium in the core instead, requiring a higher internal temperature. This shift is highly dependent on the star's initial mass, and may go through an explosive 'helium flash' if it has a degenerate core. Without enough mass, the star cannot get hot enough to fuse the helium and slowly contracts to degenerate conditions and radiates away its energy. If the initial mass is high enough, after helium burning the core will get hot enough to commence burning the carbon product of the helium burning stage [1].

The exact masses between these stellar regimes are highly uncertain. The rates of carbon fusion itself affect the boundaries of these stellar regimes. Mainly affected are the maximum mass that does not ignite carbon, the minimum mass that leads to the core-collapse supernovae, and the mass delineating formation of a degenerate carbon-oxygen-neon (CONe) core and an oxygen-neon (ONe) core [2].

There are many phenomena that the carbon fusion reaction directly affects, even in stars that do not burn carbon in their cores. Stars with $M \lesssim 9M_{\odot}$ end their lives as CONe white dwarfs, while those $9 \lesssim \frac{M}{M_{\odot}} \lesssim 11$ become ONe white dwarfs. White dwarfs in certain circumstances will undergo Nova or type Ia supernova thermonuclear explosions, of which the carbon-carbon fusion plays a large part in igniting [2].

The mechanics of these explosions are not well understood. Thus, understanding the carbon fusion reaction will help pin down how the explosion occurs, which is vital to understanding the phenomena we observe from them. This has even further effects in astrophysics, since type Ia supernovae help us understand the age of objects around them and thus serve as standard candles for the distance ladder of cosmology.

Stars that burn elements past carbon will undergo core-collapse after fusing silicon into iron, and, depending on many factors, may become a neutron star or black hole. The chemical results of the carbon burning stage affect the exact outcomes of the heavy stars and are key to understanding which stars may become neutron stars, pulsars, and black holes. Even further, the chemical makeup of exploding stars (including novae and type Ia supernovae) are released into the interstellar medium, enriching future generations of stars with the metals they have produced. Uncovering these details more exactly is vital to the stellar lifecycle and evolution of the universe.

1.2 $^{12}C + ^{12}C$ Reaction

Fusion between two atomic nuclei may produce energy (exothermic) or take energy (endothermic), which is given by the Q-Value. The Q-Value is the energy difference between the nuclear bindings of the reactant and product nuclei. For a reaction $A+B \rightarrow C+D$ with masses in atomic units (m_u):

$$Q = c^2(m_A + m_B - m_C - m_D), \tag{1.1}$$

which will be positive for exothermic and negative for endothermic reactions [1, Sec. 1.5.3]. This reaction is also commonly written as $A(B,C)D$, for example: $^{12}C + ^{12}C \rightarrow$ $^{23}\mathrm{Na} + p$ can be written as $^{12}C(^{12}C,p)^{23}\mathrm{Na}$.

Reactions can directly form the end products, but more often they first form a compound nucleus. The structure of the compound nucleus determines the energies of resonances which drastically increase the cross-section of the reaction, and thus the reaction rate. Through the compound nucleus, lighter elements can be ejected, either straight to the ground state of the nucleus or into an excited state, which may further decay to the ground state.

The ^{12}C+^{12}C reaction produces first the compound nucleus of ^{24}Mg, before continuing to different outcome 'channels'. These possible channels are:

$$\begin{array}{rl} ^{12}C(^{12}C,p)^{23}\mathrm{Na}, & ^{12}C(^{12}C,\alpha)^{20}\mathrm{Ne} \\ ^{12}C(^{12}C,\gamma)^{24}\mathrm{Mg}, & ^{12}C(^{12}C,n)^{23}\mathrm{Mg} \\ ^{12}C(^{12}C,\alpha\alpha)^{16}O, & ^{12}C(^{12}C,^{8}\mathrm{Be})^{16}O \end{array} \tag{1.2}$$

Among these, the neutron channel and the ^{16}O channels have negative Q-values (-2.62 MeV for n, -0.12 MeV for 2α, and -0.21 MeV for ^{8}Be) and are thus negligible compared to the other channels. Further, experiments suggest the γ channel also to have a negligible ratio compared to the 'p' or 'α' channels. These channels have a Q-Value of 2.24 MeV for the p-channel and 4.62 MeV for the α-channel [3].

A significant hurdle to our understanding of the reaction is the number of resonances within the compound ^{24}Mg nucleus. The high density of these states creates a difficult problem to disentangle the exact structure of resonances in the reaction, especially in the lower-energy region of the states.

Lastly, the structure of the ^{20}Ne and ^{23}Na nuclei are significant to understand their de-excitation emissions after ejection from the compound nucleus. The α_1 and p_1 emissions are the most prominent as they come from the transition from first excited state to the ground state, and there are many de-excitations to the first excited state which lead to an α_1 or p_1 emission. A table of the first five states of the nuclei and their emissions can be found in tables 1.1 and 1.2 [3]. Further, a diagram from Chieffi et al. [2, Fig. 1] can be seen in figure 1.1, showing the energy levels of the different exit channels of the reaction.

Name	Energy of Level (MeV)	Emits to States	Energy of Emission(s) (MeV)
α_0	0.0	–	–
α_1	1.634	α_0	1.634
α_2	4.248	α_1	2.614
α_3	4.967	α_1	3.333
α_4	5.621	α_1	3.987
α_5	5.788	α_1, α_0	4.154, 5.787

TABLE 1.1: First five states of ^{20}Ne

Name	Energy of Level (MeV)	Emits to States	Energy of Emission(s) (MeV)
p_0	0.0	–	–
p_1	0.440	p_0	0.440
p_2	2.076	p_1	1.636
p_3	2.391	p_1, p_0	1.950, 2.391
p_4	2.640	p_0	2.640
p_5	2.704	p_2, p_1	0.627, 2.263

TABLE 1.2: First five states of ^{23}Na

1.3 C12 Experiments

^{12}C+^{12}C experiments have been a focus of nuclear astrophysics for many decades. Due to the many products and channels of the reaction, there are many ways to study it: charged particle detection, gamma ray spectroscopy, and indirect methods. Charged particle studies have the advantage of measuring the total fusion cross section, however identifying the reaction products at low count rates can be very difficult. Gamma-ray spectroscopy has the advantage of the identification of the products, but suffers from

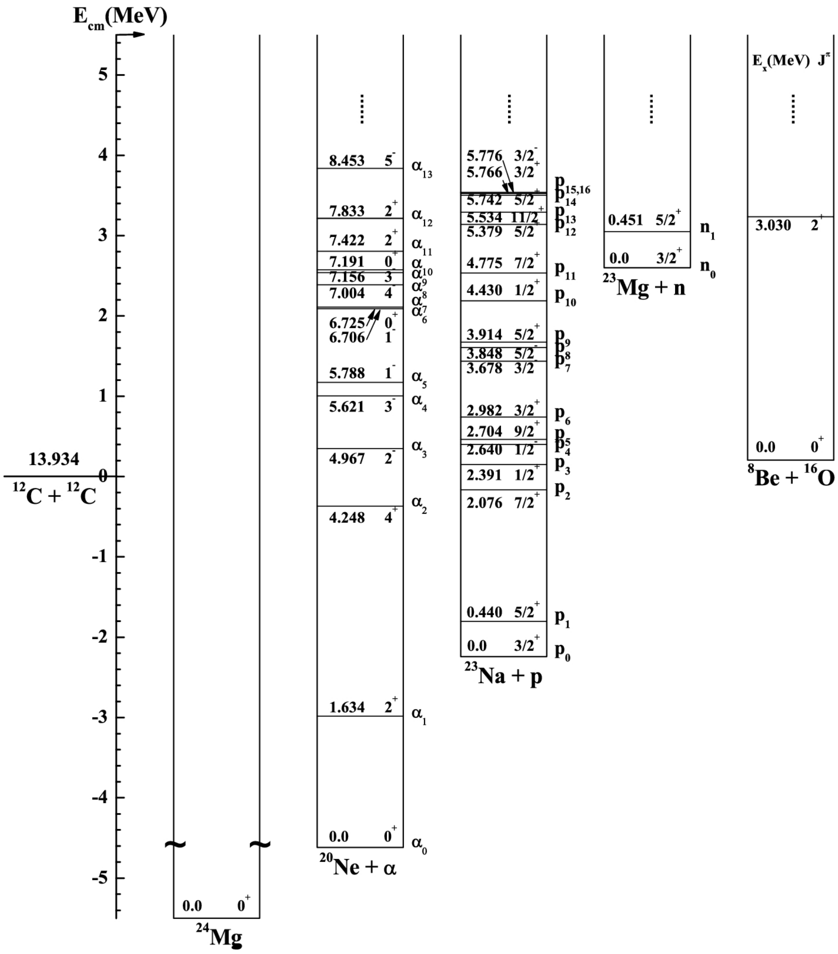

FIGURE 1.1: Energy-level diagram from fig. 1 of Chieffi et al. [2] showing nuclear levels in exit channels of the $^{12}C + ^{12}C$ reaction.

increased background and is blind to a charged particle emission directly to the ground state of the nucleus.

Both of these methods have trouble collecting data at the low energy ranges, due to extremely low reaction rates being hard to detect over background, especially cosmic radiation background. Cosmic radiation is the main source of background contamination above 2.5 MeV (see 2.10 later), and elimination of this is essential. Another issue in the measurement is the background created by reactions from the beam itself, referred to as 'beam-induced background,' which can be very hard to reduce.

Indirect methods can probe these areas more easily, at the cost of large theoretical burden and higher uncertainty. Combined, previous literature has strongly disagreed given large uncertainty in these lower energy regions, and thus new experiments must be done to clarify the picture.

1.3.1 Previous Literature

The Carbon 12 reaction has a long history starting with the scattering experiment of Almqvist et al. [4] which found resonant structure below the classical Coulomb barrier. Experiments over the years lowered the energy range probed experimentally, finding further resonant structures toward the Gamow window. These studies were contradictory as the background dominated the lower energy count rates and thus provided uncertain results [3].

Two recent studies have been important in extending our understanding of this issue. The first is Spillane et al. [5], a direct gamma-ray spectroscopy experiment, and second is Tumino et al. [6], an indirect Trojan Horse Method (THM) experiment.

Spillane et al. [5] use a High Purity Germanium (HPGe) Detector of 115% relative efficiency (compared to a standardized NaI detector) at close geometry with angle 0° from the beamline. This collects gamma rays from the de-excitation of the resulting nuclei, focusing on the 440keV and 1640keV transitions to ground state of the proton and alpha channels, respectively (p_1 and α_1 in §1.2). Along with the HPGe, they use a scintillator for veto of cosmic radiation background.

They obtained yields from an 'infinitely' thick target from center of mass energies $E =$ 2.1 MeV to $E = 4.75$ MeV, then calculated the modified S*-Factor (see §1.4.2) using a numerical derivative technique over ΔE steps of the infinite yield (detailed in §2.4). They find evidence of a strong resonance at 2.14 MeV among other unknown resonances at lower energies, which have cast doubt on previous experimental extrapolations to these lower energies, suggesting further direct studies need to be conducted.

Tumino et al. [6] use a THM experiment consisting of a ^{14}N beam onto a carbon target. This method takes a deuteron (^{2}H) as a 'spectator' particle, creating an effective ^{12}C+^{12}C reaction at lower energies, due to the relative motion of the interacting particles in the breakup of the Trojan Horse particle and the spectator particle, and varies with

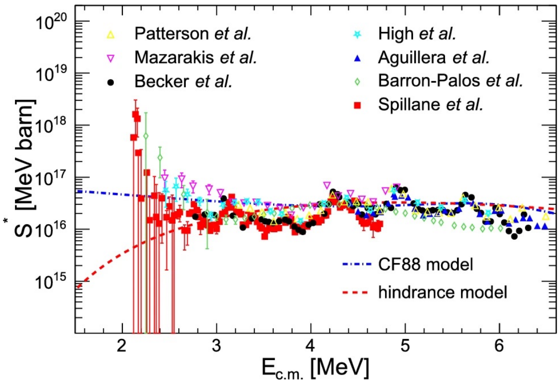

FIGURE 1.2: Chieffi et al. [2, Fig. 2] plot of S*-factor (modified S-factor) from previous results. Of importance is the highly uncertain and conflicting region below 2.5 MeV. Note Tumino et al. [6] not included in this figure

the momentum distribution of the spectator particle. With this approach, the calculated astrophysical factor is unnormalized, and must be normalized over a region to previous data. Their results suggest reaction rates significantly higher than previous results, due to many previously unknown resonances within the Gamow Window.

Additionally, two recent studies have provided further insight into these results by using a coincidence technique to only accept events in which both a charged particle and its relevant gamma emission are detected simultaneously.

Monpribat, E. et al. [7] measured the $^{12}C+^{12}C$ S*-Factor between 2.2 to 5.4 MeV with the STELLA apparatus. The coincidence technique enhances certainty in the measurements - needed for low energy extrapolation - at the cost of increased rejected events. They find reduced S-Factor in the low energy region and evidence of the 2.14 MeV resonance as suggested by Spillane et al. [5].

Tan et al. [8] at the University of Notre Dame additionally use a coincidence technique to measure the S*-Factor down to 2.2 MeV. They find similar results to Monpribat, E. et al. [7] but note a discrepancy in the α_1 channel below 3 MeV. They also compare to Tumino et al. [6] and find significant disagreement, which they suggest may be due to needed renormalization of the THM data or inclusion of Coulomb interactions in the model.

The S*-factor results of these previous studies can be seen in figure 1.2, where the region below 2.5 MeV is evidently extremely uncertain. This region is important to understand as they are the energies where stellar fusion typically takes place.

1.4 Theoretical Background

1.4.1 Gamow Peak

In a reaction, the reactants' energies are given in a thermal equilibrium, meaning their energies are described by the Maxwell-Boltzmann distribution, given by the term $e^{-\frac{E}{kT}}$.

However, the particles must also overcome the Coulomb barrier of the nuclear potential, of which the transmission through increases exponentially with higher energies. The term for this is $e^{-2\pi\eta}$ and is referred to as the 'Gamow factor' [1].

Within the Gamow factor $2\pi\eta$, the Sommerfeld parameter η can be calculated according to equation 1.3:

$$\eta(E) = \frac{e^2}{\hbar} Z_1 Z_2 \sqrt{\frac{\mu}{2E}} \tag{1.3}$$

where Z_1 and Z_2 are the two reactant atomic numbers (a factor of 36 for ^{12}C+^{12}C) and μ the reduced mass (6 for ^{12}C+^{12}C).

The Gamow peak is important because inside a star's core, where the reaction will take place astrophysically, the probability of transmission through the Coulomb barrier is very low at thermal energies. This leads to very low cross sections for the reaction, but due to the number of particles in the core, creates enough reaction rate to reach thermal equilibrium at the Gamow peak.

The product of these two terms creates a peak called the Gamow Peak, and represents the region of energies most probable for nuclear reactions in the star to occur, thus is the energy region of interest of experiments. Carbon burning typically occurs in cores of stars between 0.6 and 1.2 GK (1.2×10^9K). Figure 1.3 shows the Gamow Peak for the ^{12}C+^{12}C reaction at a temperature of 0.8GK, the vertical scale is logarithmic. Labelled are the values of the thermal energy $kT = 0.0694$MeV and peak of the probability $E_0 = 2.09$MeV, the short-dashed line shows the Maxwell-Boltzmann distribution at that temperature, the long-dashed line shows the Gamow factor, and the solid line shows the Gamow peak itself.

The most probable energy for the ^{12}C+^{12}C reaction to occur at 0.8GK being 2.09MeV exemplifies that reliable measurement is lacking in this important region, seen in section 1.3.1. Figure 1.2 shows that there is hardly any data in this vital region, and the data we have are extremely uncertain, creating a strong need for new and reliable measurements.

1.4.2 S*-Factor

To characterize the nuclear reaction rates, it is necessary to measure the reaction cross section (σ), typically given in units of barns, or 10^{-24} cm^2. To characterize the cross-section, we separate the terms into the nuclear non-exponential dependence, which we encapsulate in the astrophysical factor S(E), and the exponential dependence. If the nucleus is large enough - making the interaction radius in the nucleus large - the modified S*-Factor is used ($\tilde{S}(E)$) related to the non-modified by a factor e^{-gE} with g as the size parameter.

$$\sigma(E) = \tilde{S}(E)\frac{1}{E}e^{-2\pi\eta(E)-gE} \tag{1.4}$$

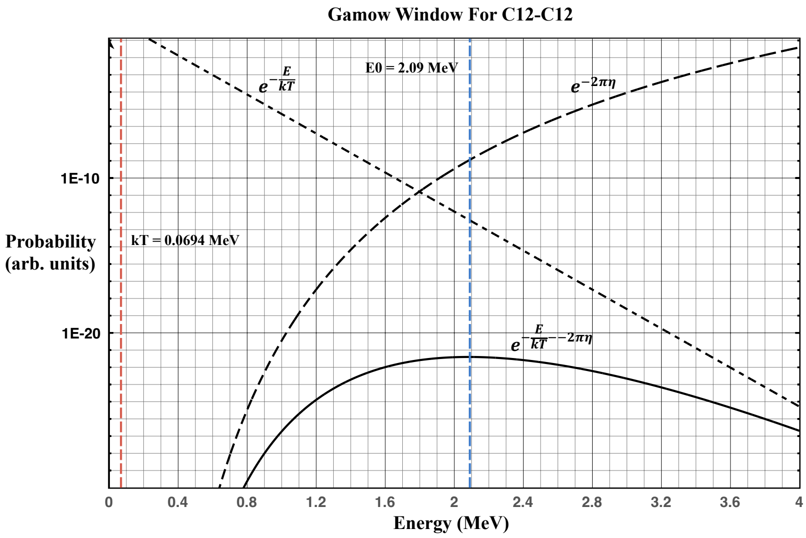

FIGURE 1.3: Gamow peak for the ^{12}C+^{12}C reaction at 0.8GK, with components labelled. The red dashed line marks the thermal energy kT, the blue dashed line the peak of the probability curve E_0, the black short-dashed line is the Maxwell-Boltzmann distribution at 0.8GK, the black long-dashed line is the transmission probability through the Coulomb barrier, and the solid black line the Gamow peak as a convolution of the two terms.

The modified astrophysical factor is used typically in literature of the $^{12}C+^{12}C$ reaction [3]. The numerical value of the size parameter for the $^{12}C+^{12}C$ reaction was calculated in Patterson et al. [9] as $g = 0.46$ MeV^{-1} and is used within this thesis for consistency with previous literature.

Chapter 2

Experiment at LUNA

2.1 Laboratory for Nuclear Astrophysics

One of the leading ways to measure low-count reactions is to perform the experiment underground. The advantage of this is the natural absorption of radiation from the atmosphere in the rock, thereby reducing the total noise. The Laboratory for Nuclear Astrophysics (LUNA) at the Laboratorio Nazionale del Gran Sasso (LNGS) is an ideal facility for this measurement [10].

LUNA has 1400m of Apennine rock above its facilities, creating a strong reduction in cosmic ray noise. With this, LUNA proposed to use the Bellotti Ion Beam Facility (IBF) 3.5 MV linear accelerator, measuring the ^{12}C+^{12}C reaction down to energies of 2 MeV in the center of mass [11].

Previously, the LUNA Bellotti IBF has been used to run experiments to study the ^{14}N(p,γ)^{15}O reaction. The experiment studied the reaction in the 0.25 to 1.5 MeV energy range, and further measured the angular distribution of the reaction at five different HPGe detector angles. The role of the Bellotti IBF and LUNA is integral in providing the experiment enough sensitivity to constrain the cross-section of the reaction at astrophysical energies [12].

This thesis will focus on the ^{12}C+^{12}C experiment at LUNA: the experimental design and results from beam irradiation down to 2MeV in the center of mass frame.

2.2 C12 Setup at Bellotti IBF

2.2.1 Particle Accelerator and Beamline

The ^{12}C+^{12}C experiment at LUNA uses the 3.5 MV accelerator at the Bellotti IBF to produce a ^{12}C^{2+} beam. The accelerator itself is a single-ended electrostatic 3.5 MV accelerator in a SF_6 environment, equipped with an electron cyclotron resonance (ECR)

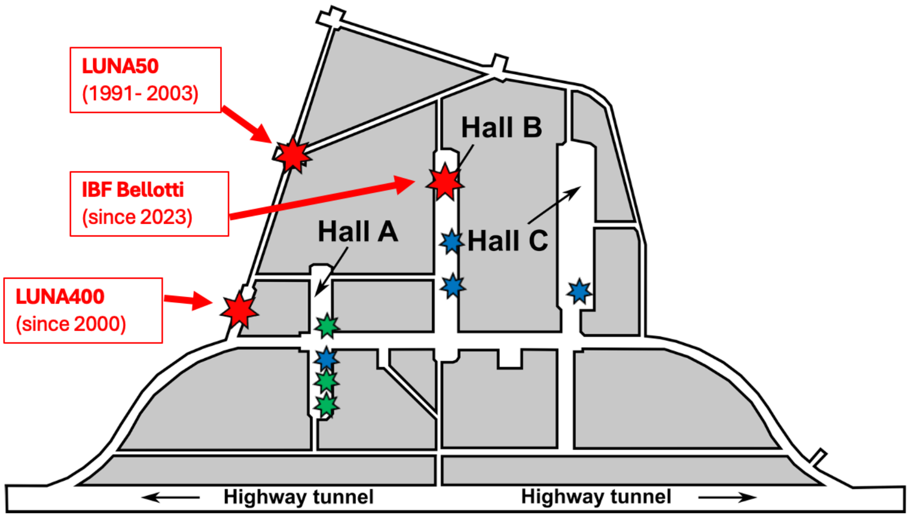

FIGURE 2.1: Map of LNGS with LUNA 400keV and the Bellotti IBF marked

ion source. It is designed to provide high terminal voltage stability and high degrees of beam stability (10^{-4}). Figure 2.2 shows the accelerator interior for reference.

The ECR ion source allows a high intensity 2+ charge state ion beam, tested for $^{12}C^{2+}$ up to 200μA of current with a typical extraction voltage of 40 kV [13]. The ion injection block is pumped to a vacuum of 10^{-6} mbar for transport to the beam line. This setup allows a beam of ^{12}C of current on target up to 100eμA at 3.5 MV terminal voltage.

The layout of the Bellotti IBF allows for two beam lines to be used from the accelerator terminus, and the C12 experiment uses the 1st beamline, using a dipole magnet to turn the beam. The end of the beamline into the interaction chamber is pictured in figures 2.3 and 2.4, showing the cold trap cryocooler, vacuum pumps, and interaction chamber with the door open.

2.2.2 Interaction Chamber

As LUNA is situated under the Gran Sasso massif deep underground, the environmental background is already severely reduced. The experimental setup is designed to reduce the background even further through both active and passive means.

The interaction chamber (figure 2.5) is surrounded by 20cm of lead shielding and 5cm of copper shielding to further reduce cosmic radiation passively. Access to the target and detector setup is granted by a moveable lead door. Further, Nitrogen flushing is performed to attenuate additional radioactive background sources. These additions suppress background by over 2 orders of magnitude [11].

While the shielding does significantly reduce environmental noise, it is noted that five peaks have been produced due to the shielding itself. These are decays stemming from ^{207}Bi and ^{60}Co, most likely due to their presence within the lead shielding. Despite this, the setup will be comparable to the most sensitive in the world [11].

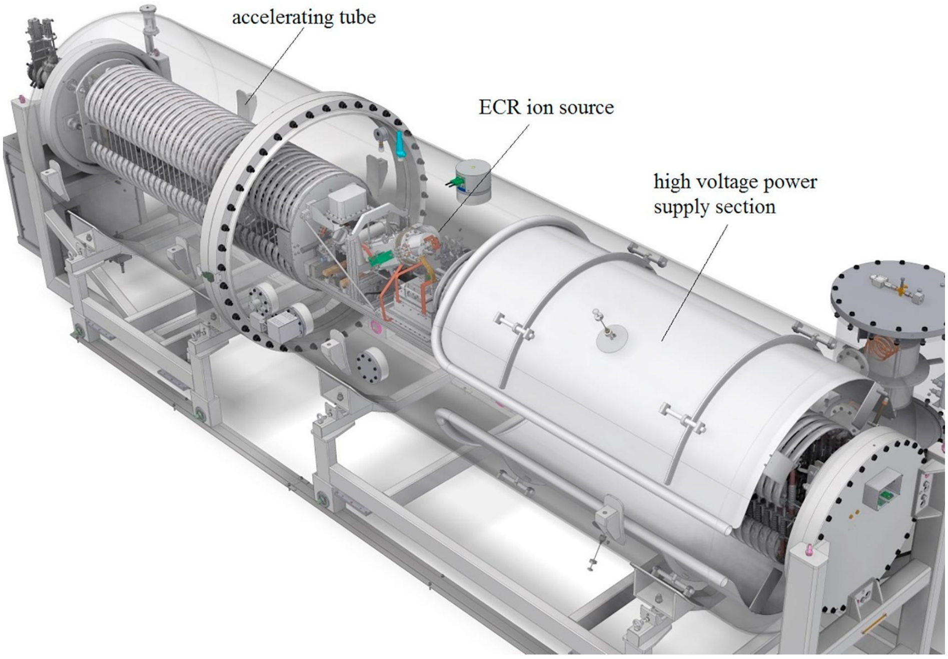

FIGURE 2.2: View inside the 3.5 MV accelerator at the Bellotti IBF from Sen et al. [13, Fig. 2]

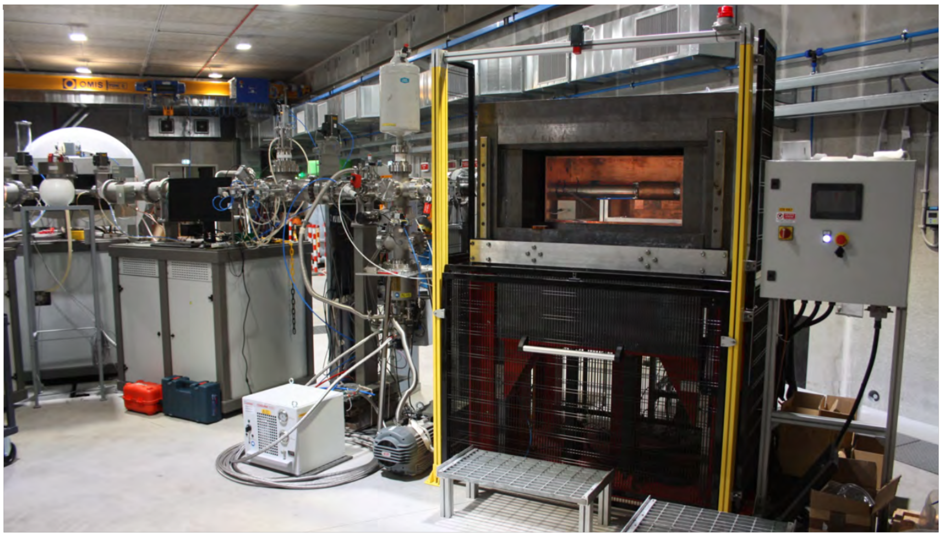

FIGURE 2.3: March 2025 image of the beamline into the open interaction chamber. Visible is a prototype of the NaI scintillator and cryocooling for the cold trap.

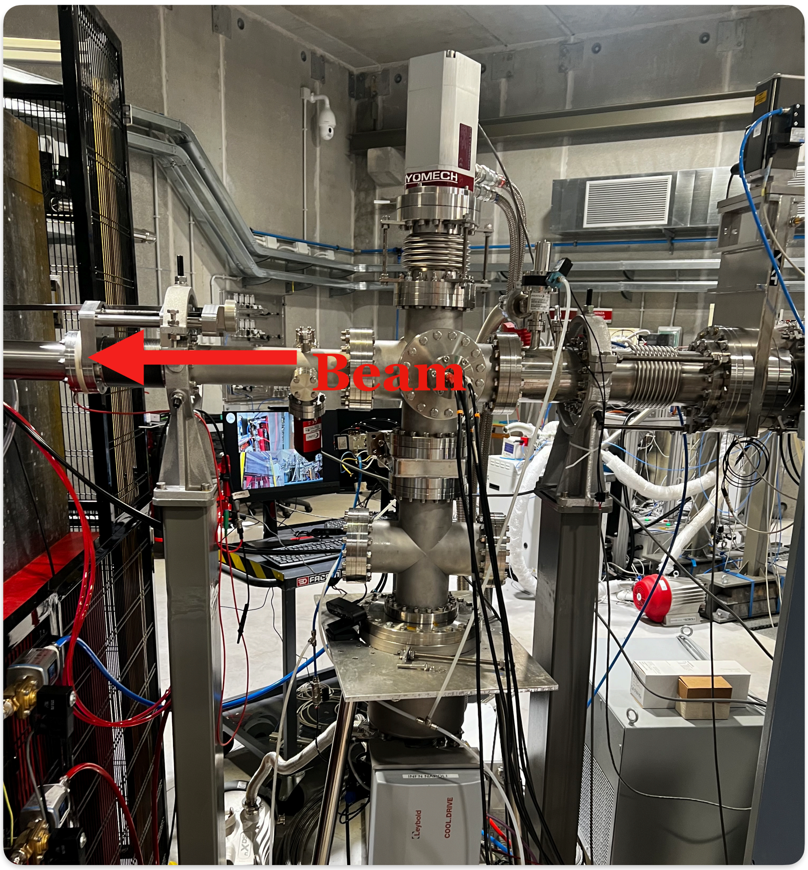

FIGURE 2.4: Image of the cold trap cryocooler and vacuum pump setup before beam enters the interaction chamber.

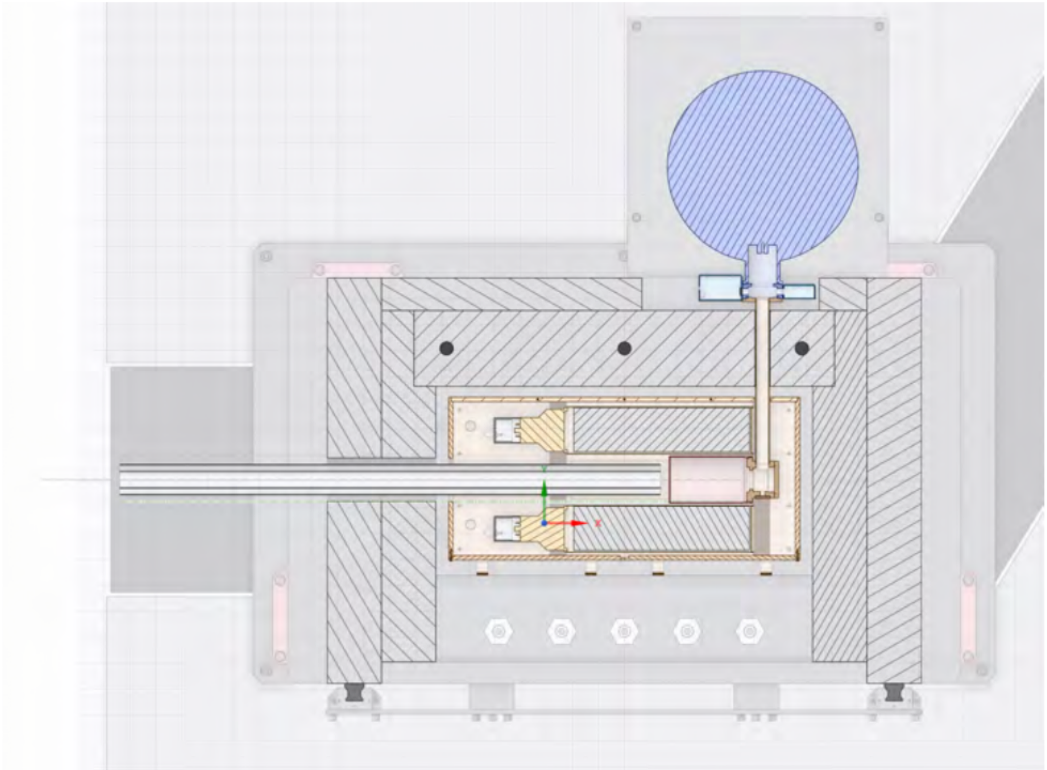

FIGURE 2.5: Cross-section from above of the interaction chamber. In red, the HPGe detector connected to cryocooler (blue), with NaI detectors around the beam. Target holder not pictured.

For maximum efficiency, both a HPGe detector at 0° close geometry and a large solid-angle NaI scintillator setup is used. The HPGe detector has a relative efficiency of 157%, making it very high efficiency compared to previous studies (Spillane, section 1.3.1)[11].

Further, the NaI scintillator setup is used as an active-veto of Compton scattering events, acting as a Compton suppression. This feature reduces the background around the 440keV peak by a factor greater than 2 [11].

Also inside the interaction chamber is the copper cold trap, cooled to liquid Nitrogen temperatures to enhance the vacuum to about 10^{-7} mbar along with the normal scroll and cryogenic pumps. The cold trap additionally will be connected to negative voltage to act as an electron suppressant. With this negative charge, electrons emitted against the beam line from the beam hitting the target will be pushed back to the target instead of lost.

Lastly is the target holder (figure 2.6), which features a liquid cooling backing to keep the target cool enough to withstand beam impingement for long durations. The holder is made of tantalum and can be adhered to the target using Master Bond EP3HTS-TC glue which can dissipate heat and conduct electric current exceptionally well. The glued target must be cured in an oven at 150°C for 15-20 minutes, and given another oven treatment post-cure at 150°C.

Additionally, the backing is connected to the holder by many pins which allow the water to flow over, increasing thermal contact and heat dissipation. This was made

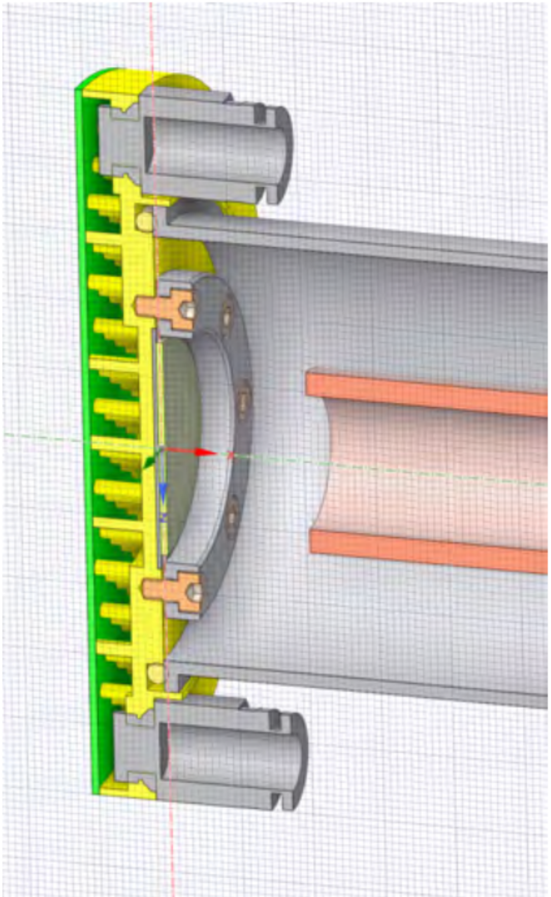

FIGURE 2.6: Diagram of the Tantalum target holder (without target). Visible is the cold trap (right) and the pin-mounted water cooling structure.

using LPBF (Laser Powder Bed Fusion) technology.

2.3 Targets

There are many methods of making carbon targets, and tests were carried out at the Felsenkeller laboratory in Dresden to determine the best for our purposes. Target selection was done to minimize the amount of degradation and maintain stability of the targets under beam bombardment and effectiveness of the glue. However, the target holder was of a different design than at LUNA, and the beam power available at Felsenkeller is lower than at LUNA [14].

The tested targets include a ZXF and AXF sintered graphite, a glassy carbon, and an HOPG type target. Each of the targets has different densities and thermal conductivity, which affect the target's ability to withstand beam impingement. The tests allowed us to make the choice of the AXF and ZXF targets manufactured by Entegris POCO since the glassy carbon and HOPG targets had fewer contaminants but had not been able to withstand the beam during bombardment. An image of a ZXF target after beam bombardment can be see in figure 2.7, evidencing the targets stability.

In the experiment, different individual targets were used and kept track of to measure

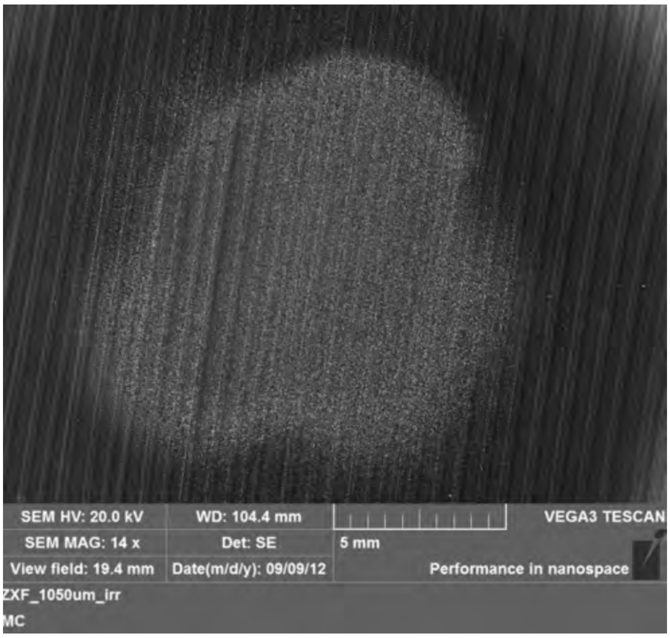

FIGURE 2.7: Zoomed image of the beam spot on a ZXF target after beam bombardment at LUNA with total accumulated charge of 5.828 Coulombs. Taken with a scanning electron microscope.

the contamination and stability of the different targets over the time of beam bombardment. In monitoring the contamination of the target, we looked at the ^{1}H and the ^{2}H beam-induced-background (BiB). In the ^{12}C+^{12}C experiment, the ^{1}H emits at 2420 keV gamma and the ^{2}H emits a 3100 keV gamma (see table 3.5).

Thus, by monitoring these regions for emission, we can understand how much BiB the target is creating from hydrogen contamination. Overall the hydrogen contamination decreases as the target is irradiated, and is affected by the moisture content of the room. Thus, baking the targets in an oven reduces this contamination, and the targets must be handled carefully to reduce the ambient contamination. These results are evident in figure 2.8, showing target contamination yield of sequential runs.

2.4 Reaction Yields

The yield of an experiment is an easy calculation to make given the number of reactions and number of particles in the beam, and is related to the cross-section at that beam energy [1]. Given an infinitely thin target:

$$Y(E_0) = \frac{N_{\text{reactions}}}{N_{\text{beam}}} = \sigma(E_0) n \Delta x \tag{2.1}$$

with n as the number density of target particles and Δx the thickness of the target. Of course, experimentally it is not so easy.

Firstly, we do not know exactly how many reactions there are, and must estimate using measured counts, detector efficiencies, and branching ratios. It also depends on the

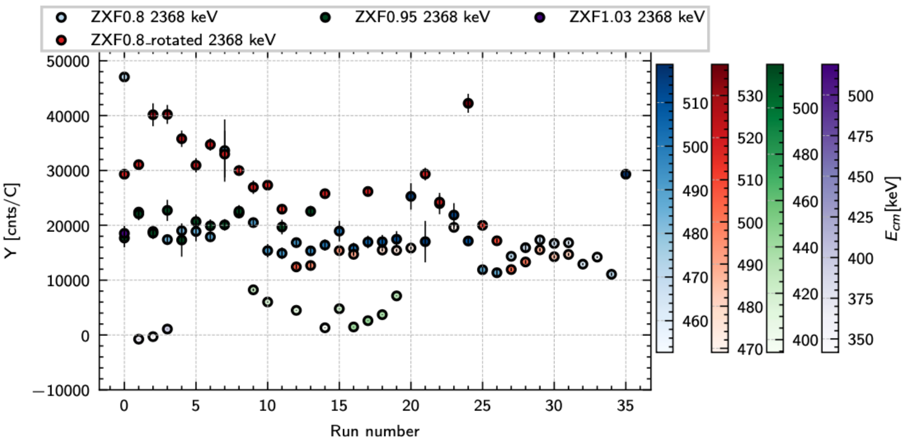

(A) Hydrogen contamination over runs of different targets

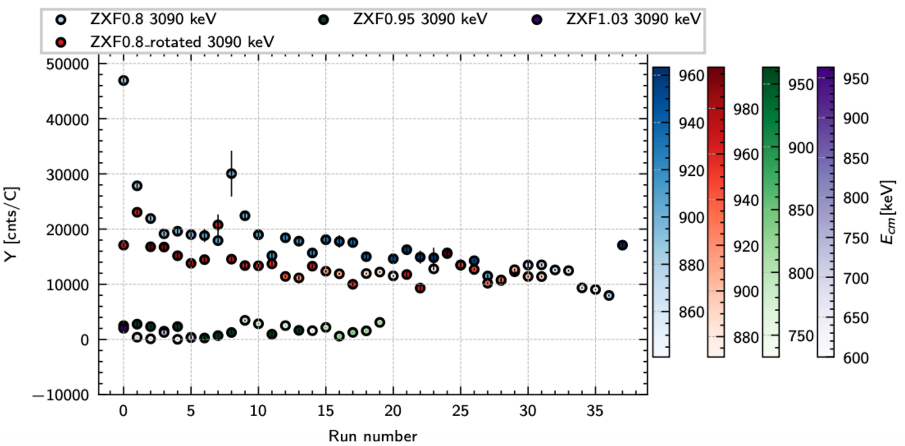

(B) Deuterium contamination over runs of different targets

FIGURE 2.8: Contaminant yield trends over sequential runs. Visible is the reduction of the yield after initial runs. ZXF0.95 and ZXF1.03 were baked beforehand and show significant reduction to the contaminant yields

angular distribution $W(E, \theta)$ of the reaction products, which we take as 1 in this thesis as an approximation.

$$N_{\text{reactions}} = \frac{N_{\text{counts}}}{\eta \cdot b} \tag{2.2}$$

with η as the efficiency of the detector, b as the branching ratio, and N_{counts} as the total integrated counts detected. The number of particles in the beam is approximated by taking the deposited charge on the target over the experimental run and dividing out the charge of each incident particle ($2e$ in the case of $^{12}C^{2+}$, where e is the elementary charge of an electron).

Secondly - and most importantly - the target is not infinitely thin. Since the target must have some amount of thickness, the beam will lose energy inside the target and represent a range of energy values of the cross section as it passes through the target reacting [1]. Thus, we must set up an integral for the yield across the target thickness:

$$Y(E_0) = \int_{E_0 - \Delta E}^{E_0} \frac{\sigma(E)}{\epsilon(E)} dE \tag{2.3}$$

with $\epsilon(E)$ as the stopping power for the particle at energy E which relates the Δx of the target thickness to a ΔE. It is important to carefully note that the stopping power and beam energies are expressed in the same reference frame, since typically beam energy is expressed in the center of mass frame and the stopping power in the laboratory frame.

However, for even thicker targets the beam may stop entirely in the target, meaning we have an 'infinite' yield:

$$Y^{\infty}(E_0) = \int_{0}^{E_0} \frac{\sigma(E)}{\epsilon(E)} dE \tag{2.4}$$

which can be used to calculate the cross section [3] as:

$$\sigma(E_0) = \frac{\epsilon(E_0)}{\eta} \frac{dY^{\infty}(E_0)}{dE} \tag{2.5}$$

Finally we can use equation 1.4 to relate this to the desired modified astrophysical factor:

$$\tilde{S}(E) = \frac{E\epsilon(E)}{\eta} e^{2\pi\eta + gE} \cdot \frac{dY^{\infty}(E_0)}{dE} \tag{2.6}$$

2.4.1 Infinite Yield Curves

The effect of the target being infinite on the yield curve is the integration of all resonances below each energy, as is obvious from equation 2.4. This is due to each resonance being contained within the ΔE of the slowing down beam as it passes through the target.

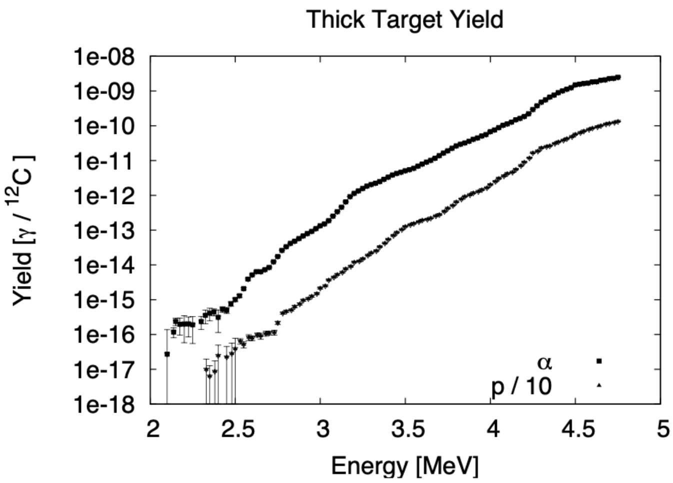

FIGURE 2.9: Figure 3.3 from Spillane et al. [5] showing infinite target yields for their $^{12}C+^{12}C$ experiment. The curve clearly creates the 'step' feature due to the beam slowing in the target integrating the lower resonances

Thus, we see a 'step' feature as the beam energy reaches a resonance, as can be seen in figure 2.9 from Spillane et al. [5, fig. 3.3] showing their infinite yields of the $^{12}C+^{12}C$ experiment.

2.5 HPGe Detectors

Experiments which use a HPGe detector (as LUNA, Spillane et al. [5]) analyze spectra from gamma rays absorbed in the detector crystal. The germanium crystal is a semiconductor, which 'promotes' electrons from the valence band to the conduction band given energy deposition. These free electrons then are collected at quick intervals by a diode [15].

These detectors are very sensitive due to their small band gap, creating higher energy resolution due to a larger number of electron-hole pairs produced being collected per unit of energy deposited. To work as detectors, they must be cooled to very low temperatures (liquid nitrogen) to keep the extra thermal energy from creating noise in the detector.

There are many processes in which the energy can be transferred, which affect the resulting output of the detector. The first is the photoelectric effect, in which the full energy of the photon is absorbed into the detector, creating free charges proportional to the amount of energy. This creates a 'photopeak' at the energy of the gamma ray, and is ideal for understanding the origin of the gamma ray [16].

Secondly is Compton scattering within the detector which deposits only some of the energy of the gamma ray. The Compton scattering formula (equation 2.7) shows that the energy deposited depends on the angle of scattering, and the maximum deposited energy occurs with scattering angle $\theta = 180°$. Thus, we can expect a Compton 'continuum' to occur below each photopeak, adding to the background of any peak in that region [16].

$$E_{\gamma_2} = \frac{E_{\gamma_1}}{1 + \frac{E_{\gamma_1}}{m_e c^2}(1 - \cos\theta)} \tag{2.7}$$

Lastly, given a photon with energy above $2m_e c^2 = 1.022$ MeV, the photon can undergo pair production in the Coulomb field of an atom, creating an electron and positron pair. The positron then can annihilate with an electron and generate two 0.511 MeV photons, one or both of which can be absorbed within the detector. If one or both photons are not absorbed, the total recorded energy of the photon will have 0.511 or 1.022 MeV missing as a result. This results in single- or double-escape peaks from the energy of the originating gamma-ray [16].

The photoelectric effect dominates at lower gamma energies, up to about 0.2 MeV when Compton scattering becomes more prominent. Compton scattering dominates up to about 8 MeV, after which pair production dominates. The exact energies of these regime changes depend on the atomic number (Z) of the absorber material, of which I have reported numbers for Germanium ($Z = 32$) [15]. This means, at the typical gamma energies in a $^{12}C+^{12}C$ experiment (440 keV and 1634 keV), Compton scattering dominates and will create extra noise in the detector.

A HPGe detector has much better energy resolution than a scintillator, allowing experiments to more accurately distinguish each gamma. This is important when two emissions are relatively close, and for analysis of the peak shape in the case of broadening effects. A scintillator has much worse energy resolution (80keV NaI vs 2keV HPGe for a 1332 keV gamma), but has much higher total detection efficiency to absorb gamma energy, is more available in larger volumes, and can be operated at room temperatures [16, Section 10.14].

2.5.1 Detector Noise and Sensitivity

For the LUNA C12 experiment specifically: Gesuè et al. [11] performed an analysis on the background and performance of the HPGe detector of the setup. Firstly, they do a background study to determine the count rate registered in the detector expected without any source or beam. They find the full setup (underground, 15cm lead and 5cm copper shielding, nitrogen flushed) decreases the count rate by over three orders of magnitude, see figure 2.10. To note is that the experiment added 5cm of lead shielding for the full experiment.

They estimate the expected count rates in the 440 keV region of interest to be 3.6(1) keV^{-1} d^{-1} and in the 1633 keV region to be 0.44(3) keV^{-1} d^{-1}. To understand how this compares to the expected counts of the $^{12}C+^{12}C$ reaction, they additionally performed a sensitivity study based on previous studies of the reaction [11].

Considering cross-sections from previous experiments and a 30 day beam time, the lowest measurable beam energies in the center of mass frame are 1.7MeV to 2MeV. They note

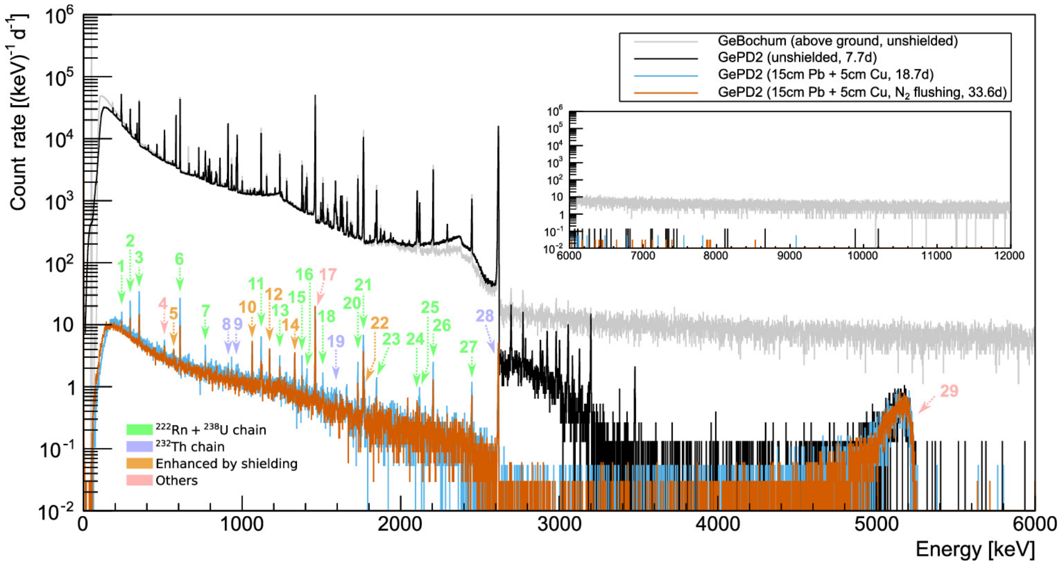

FIGURE 2.10: Gesuè et al. [11, Fig. 2] analysis of background under different shielding. Grey is unshielded above ground, and the rest are underground: black is unshielded, blue is shielded, and orange is shielded and nitrogen-flushed. Note that only 15cm of Pb shielding was used in this study, where 5cm has been added since.

that the estimation largely depends on the cross-section assumed and that the analysis was performed without the added NaI scintillators.

2.6 Doppler Effect

The Doppler effect is the lengthening or contracting of wavelengths due to the emission source not at rest in the reference frame of the observer. Since the emissions of the decay radiation from the product nuclei of the $^{12}C+^{12}C$ reaction have some kinetic energy due to the energy of the beam, this energy will be seen in our resulting spectra as broadened peaks.

The Doppler change is given by the equation:

$$\Delta E_{\mathrm{Dop}} = \frac{v}{c} E_\gamma \cos\theta \tag{2.8}$$

with v as the speed of the emitting particle, c as the speed of light, E_γ as the energy of the emitted gamma, and θ as the velocity vector angle from the detector. There are many factors which impact the resulting Doppler peak shape, making the shape highly variable on the kinematics and other parameters of the emission.

Importantly, we must consider the stopping power. If the stopping power of the resulting nucleus is large enough compared to the lifetime of the excited state, then the nuclei will have stopped in the target as the emission occurs, creating only small Doppler effect. In this case, we see a 'spike' in the broad peak at the E_γ due to this effect.

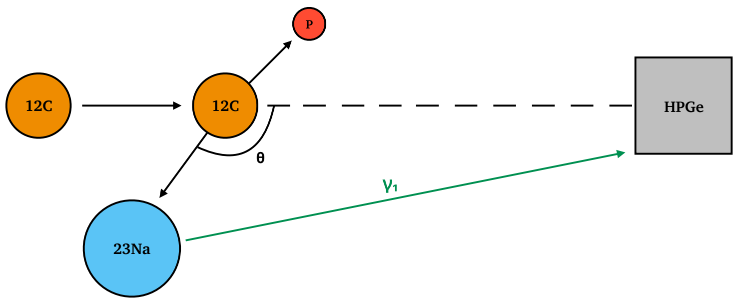

(A) Diagram of redshifted emission of a ^{12}C(^{12}C,p)^{23}Na reaction producing a γ_1.

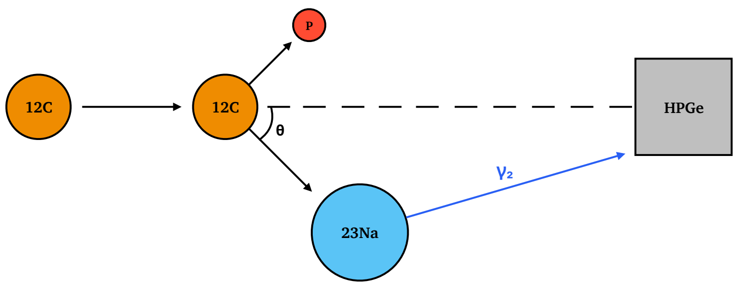

(B) Diagram of redshifted emission of a ^{12}C(^{12}C,p)^{23}Na reaction producing a γ_2.

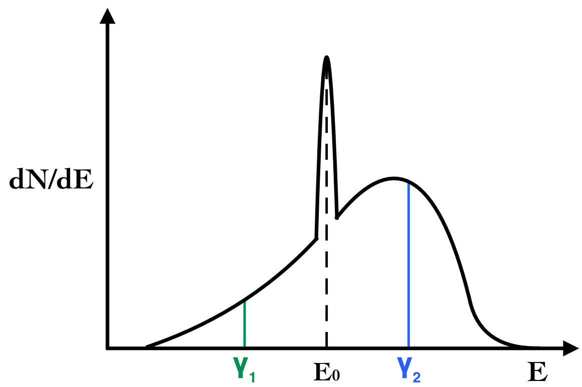

(C) Diagram of spectrum produced from a range of θ, with E_0 as the E_γ and γ_1 and γ_2 from above.

FIGURE 2.11: Diagram of Doppler effect on spectral peak of gamma ray in experiment.

Chapter 3

Data Analysis

3.1 HPGe Efficiency

3.1.1 Detector Efficiency

Since not all photons will interact in the detector or deposit their full energy, it is important to characterize an experiment's detector's ability to absorb incoming gamma rays into an efficiency function $\eta(E, d)$. This function will depend on the energy of the target-emitted gamma ray (E) and the distance of the detector from the target (d), and further will be split into a total efficiency to absorb the gamma η_{tot} at any energy and a photopeak efficiency η_{ph} to absorb the gamma at full energy specifically.

This is done by taking well-known gamma-ray producing sources and comparing the counts registered in the detector versus how many are expected from the source. Obviously, the counts registered will be related to the amount of the solid angle the detector takes up (hence the distance dependence). From sources with known activity, it is easy to calculate the efficiency of a certain gamma ray. Since the efficiency is defined as the ratio of the number of counted gammas over the number of emitted gamma rays, we can calculate in the ideal case using equation 3.1:

$$\eta = \frac{N_{\text{count}}}{N_{\text{emit.}}} = \frac{N_{\text{count}}}{A \cdot \Delta t \cdot b_i} \tag{3.1}$$

where A is the activity at time of measurement, Δt is the duration of the measurement, and b_i is the branching ratio of that specific gamma [16].

Figure 3.1 shows the decay modes of the ^{60}Co and ^{137}Cs sources from the National Nuclear Data Center (NNDC). ^{137}Cs is considered ideal because there is only one gamma emitted, meaning there are no summing effects from other gamma-rays. Summing effects are when the emission of two gamma rays (typically in cascade) are registered in the detector within the detector timing window, registering both as a single gamma ray.

Summing effects can be split into summing-in and summing-out. Summing-in is where a coincidence deposits energy in the photopeak of another gamma, which is erroneously counted as part of the peak. Summing-out is when the coincidence creates the appearance of a count with energy of the two summed and is thus removed from the counts of the desired peaks.

The summing-in effects of ^{60}Co can be corrected with Eqns. 3.2 and 3.3, which describe the number of gammas accumulated in a peak as a function of the number of source decays (N_{decays}), branching ratios (b), and efficiencies (η_{tot}, η_{ph}) of two gammas emitted in cascade [17]. Here, γ_1 is emitted before γ_2 in sequence:

$$N(E_{\gamma,1}) = N_{\text{decays}} b_1 \eta_{\text{ph}}(E_{\gamma,1})(1 - b_2\eta_{\text{tot}}(E_{\gamma,2})) \tag{3.2}$$

$$N(E_{\gamma,2}) = N_{\text{decays}} b_1 b_2 \eta_{\text{ph}}(E_{\gamma,2})(1 - \eta_{\text{tot}}(E_{\gamma,1})) \tag{3.3}$$

^{60}Co also has a very small probability of a single gamma de-excitation. Equation 3.4 accounts for this possibility with its branching ratio b_3 and the possibility of summing-in from the cascade:

$$N(E_{\gamma,3}) = N_{\text{decays}}(b_3\eta_{\text{phot}}(E_{\gamma,3}) + b_1 b_2 \eta_{\text{ph}}(E_{\gamma,1})\eta_{\text{ph}}(E_{\gamma,2})) \tag{3.4}$$

These sources provide a reasonable parameterization of the detector's photopeak efficiency. However, to extrapolate to higher energies, higher energy photon calibrations are needed, which can be provided by the ^{14}N(p,γ) reaction. Since there are many levels to the compound ^{15}O nucleus, equations 3.2-3.4 must be generalized to any number of levels and cascades. Further, since the activity of the reaction is unknown, the N_{decays} variable must be swapped with a free parameter of reaction rate, R [17]. To simplify, the cascades of 763keV to 6971keV and 1380keV to 6176keV are used; see figure 3.2 for the level scheme of the ^{15}O compound nucleus.

To parameterize our fit, we use a distance function (equation 3.5) and an expansion of the exponential logarithmic energy (equation 3.6). These allow us to parameterize both the distance and energy dependence of the efficiency function, and will require data at different gamma energies and detection distances.

$$D(d; E_\gamma) = \frac{1 - \exp\left(-\frac{d+d_0}{d_1+d_2\sqrt{E_\gamma}}\right)}{(d+d_0)^2} \tag{3.5}$$

$$\eta_{\text{ph}}(d; E_\gamma) = D(d; E_\gamma)\exp[a + b\ln(E_\gamma) + c\ln^2(E_\gamma)] \tag{3.6}$$

d is the detector distance and d_0, d_1, d_2, a, b, and c are free parameters for the fit [17][19].

One issue we run into is the calculation of the total efficiency of the ^{14}N data, since the total rate is also a parameter. We can avoid this by using a relative approach, assuming

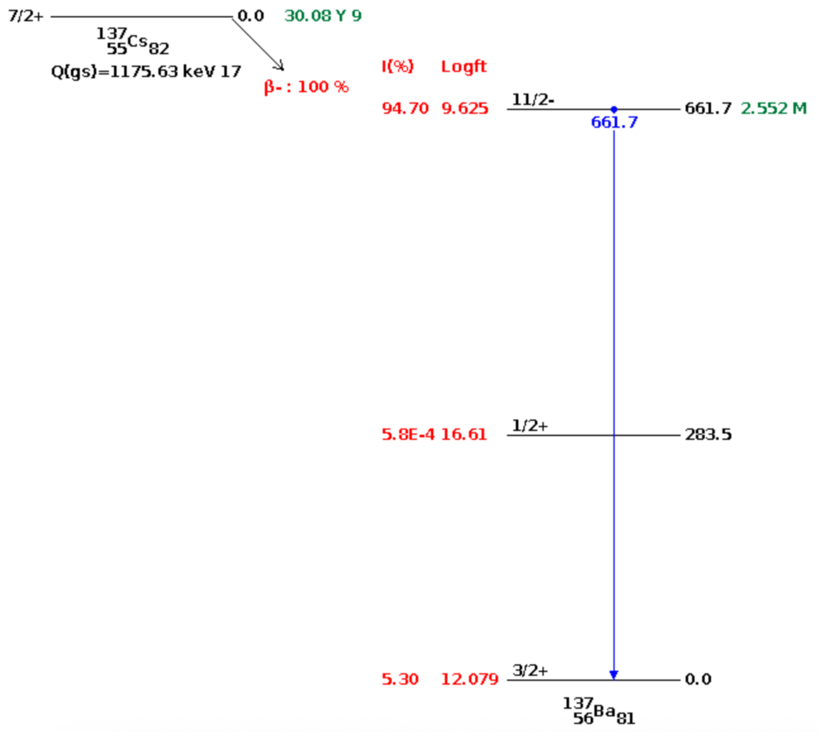

(A) ^{137}Cs Single Emission

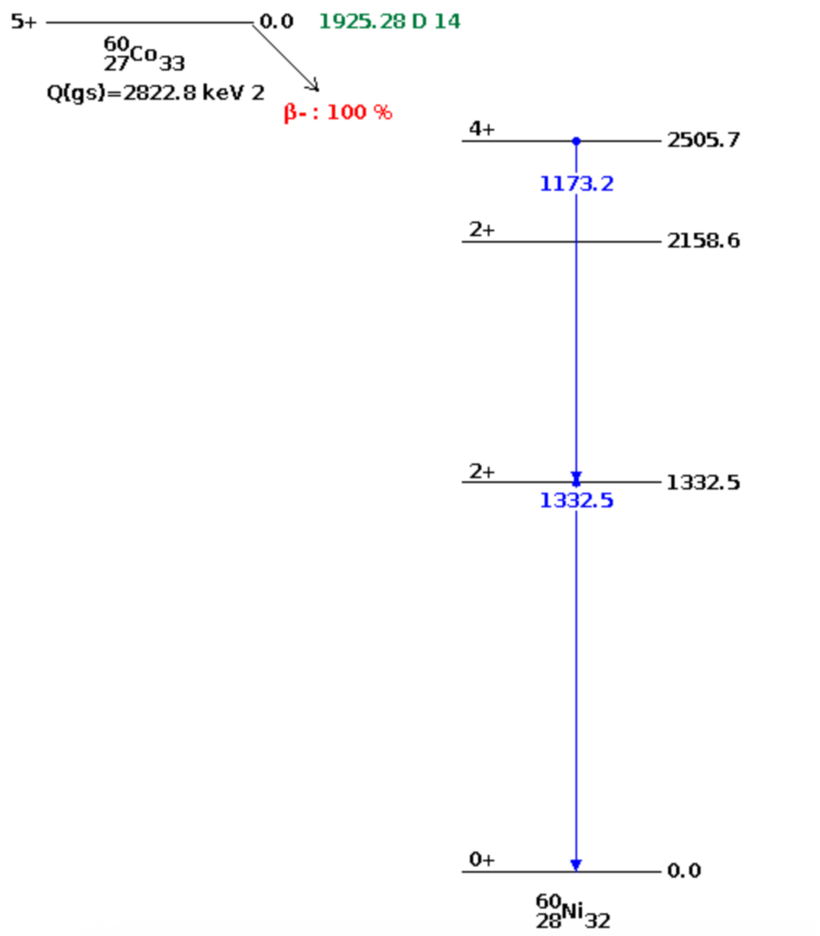

(B) ^{60}Co Cascade

FIGURE 3.1: Decay Schemes for ^{60}Co and ^{137}Cs; from NNDC [18])

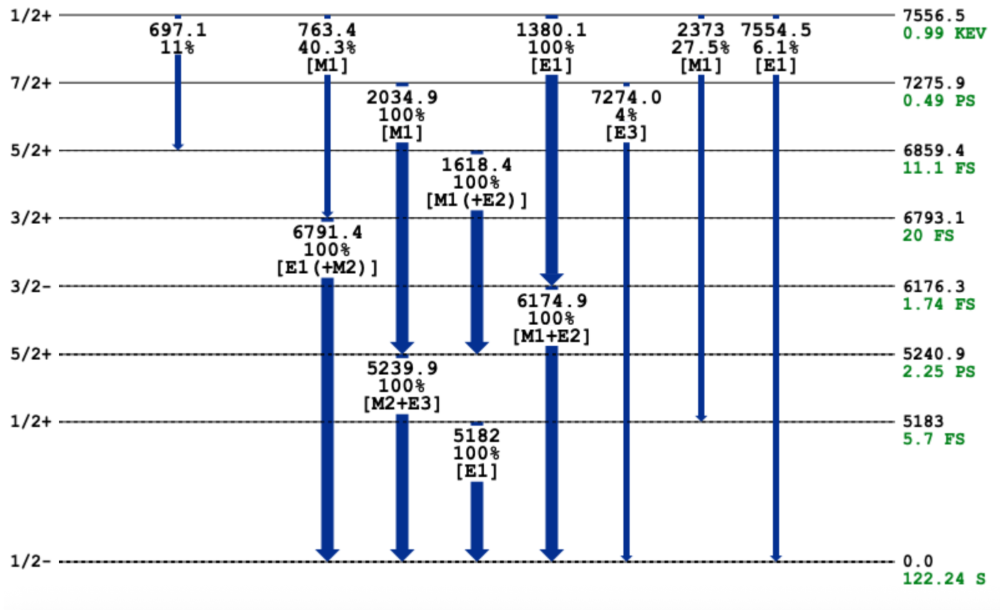

FIGURE 3.2: Level scheme of ^{15}O, from NNDC [18]

all decays go through the secondary photon given the first. In this way the ratio of the two gamma ray integrated counts (e.g. $\frac{N(763keV)}{N(6791keV)}$) are equal to the ratio of their efficiencies, and the reaction rate parameter will divide to 1.

Given one parametric fit for the lower energy source photons, the upper energy photopeak efficiency can thus be calculated from the ratios as $\frac{N_1}{N_2} \cdot \eta_2 = \eta_1$. It is possible to use the fitted parameters to calculate the predicted photopeak efficiency and allow the parameters to adjust to match the two. In essence, we are using the ratio to estimate what the high energy efficiency should be given the fit for the lower energy efficiency, then matching the parameterized equations for the predicted high energy efficiency; it is a complicated fitting procedure.

Alternatively, we can use a third equation (equation 3.7) to parameterize the total efficiency ratio to back-calculate the yield for each photon given the equations 3.2 and 3.3. Then we compare the calculated and the observed yield as the errors for our fit. We thus must introduce three more free parameters to create this extra parameterization: k_1, k_2, and k_3:

$$\ln\left(\frac{\eta_{\text{ph}}}{\eta_{\text{tot}}}\right) = k_1 + k_2 \ln(E_\gamma) + k_3 \ln^2(E_\gamma) \tag{3.7}$$

This method allows a more robust parameterization, at the cost of the extra free parameters creating a more difficult fitting procedure with the same amount of points. I use the extra parameters method in section 3.1.2 to perform the analysis in this thesis.

3.1.2 Efficiency Fit

In October 2025, data was taken at the Bellotti IBF at LNGS for the purpose of characterizing the HPGe detector efficiency. γ-spectra were gathered for a ^{137}Cs and a ^{60}Co source, as well as the 259keV resonance of the ^{14}N(p,γ) reaction. These were done at three different distances: 1mm, 40mm, 80mm. A summary of this data can be seen in table 3.1. The sources were calibrated at the Physikalisch-Technische Bundesanstalt on the 1st of July, 2016 with activities 6.46 ± 0.07 kBq for the ^{137}Cs and 9.01 ± 0.07 kBq for the ^{60}Co. The calculated yields for each of the runs done can further be seen in table 3.2.

Figure 3.3 shows the γ-spectra of a single run of the three calibration methods. The spectra are measured in detectors channels and must be calibrated, which is simple given the known energies of the peaks. Though a polynomial fit can be used for higher accuracy, a simple linear model works well for our purposes. The peak areas can easily be found by integrating in ROOT using a background averaged over the bins surrounding the peak. A zoomed-in spectrum of the ^{14}N peaks can be seen in figure 3.4.

The yield is calculated for sources simply as $\frac{N_\gamma}{N_{\text{decays}}}$, while for the ^{14}N(p,γ) reaction we must use $\frac{N_\gamma c}{C}$ where c is the ion charge and C is the total accumulated charge on the target. The peak area error additionally is calculated as:

$$\text{var}(A) = \sum_{i=L}^{U} C_i + \frac{n^2}{4m^2}\left(\sum_{i=L-m}^{L-1} C_i + \sum_{i=U+1}^{U+m} C_i\right) \tag{3.8}$$

where L is the peak lower bound, U is the peak upper bound, m is the number of background bins on each side, n is the number of bins in the peak region, and C_i is the number of counts in bin i [16, Eqn. 5.40].

Run	Date	Length (s)	Source	Distance (cm)
633	20/10/2025 14:18	900	^{14}N(p,γ) 286keV	0.1
634	20/10/2025 16:37	2640	^{14}N(p,γ) 286keV	4
635	20/10/2025 18:19	1440	^{14}N(p,γ) 286keV	8
676	24/10/2025 15:43	720	^{137}Cs	0.1
677	24/10/2025 16:00	2580	^{137}Cs	4
678	24/10/2025 16:44	1380	^{137}Cs	8
679	24/10/2025 17:17	1860	^{60}Co	8
680	24/10/2025 17:50	720	^{60}Co	4
681	24/10/2025 18:06	420	^{60}Co	0.1

TABLE 3.1: Table of data for calibration of HPGe detector

To fit the data, initial parameters are chosen which approximate the function shape, then a preliminary fit is done in the spreadsheet itself, using a χ^2 loss function using residuals weighted by the yield error to evaluate the performance of the parameters against the data. Then, the data is moved to Python for a more complete fit using `SciPy`'s `optimize` package, specifically the `leastsquares` function.

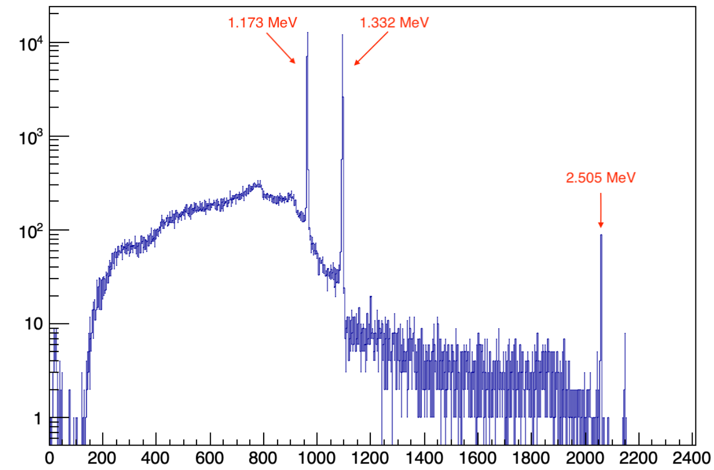

(A) Spectrum of Cobalt

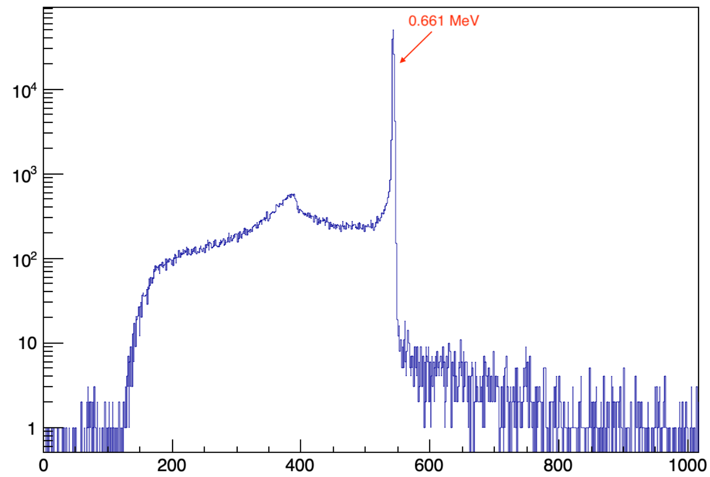

(B) Spectrum of Caesium

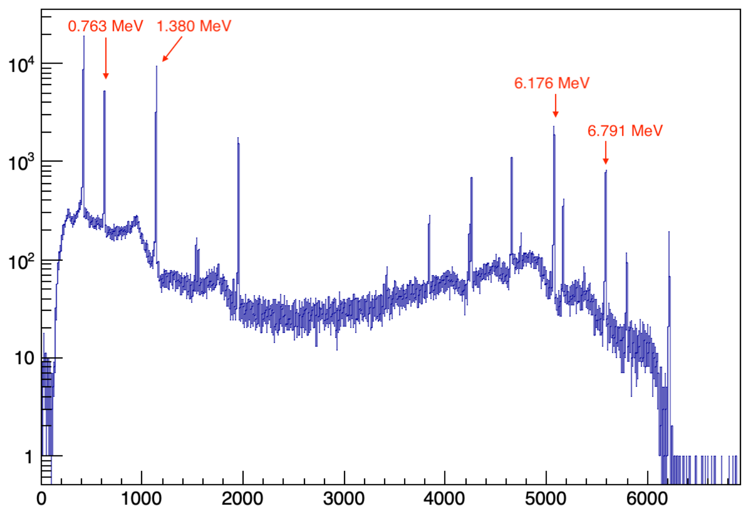

(C) Spectrum of ^{14}N(p,γ)

FIGURE 3.3: γ-spectra of the efficiency measurements in logarithmic scale with relevant peaks labelled with energy. Note the x-axis is in channels, not energy.

Run	Peak (MeV)	Yield	Run	Peak (MeV)	Yield
633	6.7914	0.073396217	676	0.6617	0.03738013
633	6.1763	0.20014673	677	0.6617	0.01425269
633	1.3801	0.597024183	678	0.6617	0.0073923
633	0.7634	0.301246057	679	1.173	0.00726208
634	6.7914	0.033030614	679	1.332	0.006914888
634	6.1763	0.090565805	680	1.173	0.01355841
634	1.3801	0.267075906	680	1.332	0.013019526
634	0.7634	0.131872538	681	1.173	0.030623072
635	6.7914	0.017132261	681	1.332	0.029469364
635	6.1763	0.049568494			
635	1.3801	0.140354451			
635	0.7634	0.072523383			

TABLE 3.2: Table of calculated yields for each peak in the calibration of the HPGe detector

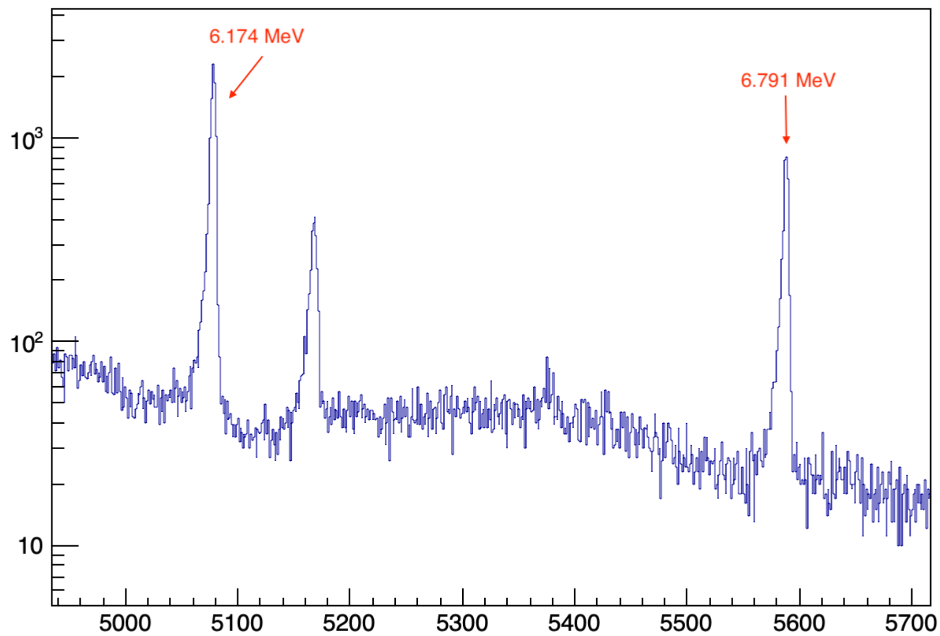

FIGURE 3.4: Zoom-in on ^{14}N 6.791 MeV and 6.176 MeV regions of interest. Compton background decreases with energy due to less peaks above these energies.

To accomplish the complicated fit in Python, I construct generator function to build the yield functions for each data point, which are used by the `leastsquares` function to calculate the yield for each de-excitation gamma. The results can be seen in table 3.3, along with both the χ^2 and reduced χ^2 of the fit.

The fit results in a reduced χ^2 value of 40.96, which is very large. However, with this complicated fit with many parameters, it represents a typical and reasonable result. Further the results of k_1 and k_2 being 0 seems perhaps suspect, but the fit converges to these values given a large range of initial input values, as well as represents the significantly lowest χ^2 result of any fitted model.

3.1.3 Efficiency Errors

The output of the `leastsquares` function contains a Jacobian described as the "Modified Jacobian matrix at the solution, in the sense that $\mathbf{J^T J}$ is a Gauss-Newton approximation of the Hessian of the cost function" [20]. With this, I can calculate the Hessian of the fit which is useful as $\mathbf{C} = \mathbf{H^{-1}}$ is the covariance matrix which gives the variance on the parameters along the diagonal, tabulated in table 3.3.

Parameter	Best Fit	σ
d_0	4.107533	0.693540
d_1	1.064187	2.361094
d_2	5.470458	3.137373
a	0.288508	0.048156
b	-0.226169	0.115523
c	-0.102515	0.024593
k_1	0	3.533500
k_2	0	4.116516
k_3	-0.757337	2.090469
R	38.332702	1.852444
χ^2	χ^2/dof	
573.44	40.96	

TABLE 3.3: Best Fit values after least-squares fitting with Gauss-Newton-approximated errors

To further estimate errors on the function's calculated efficiency values, I use a Markov Chain Monte Carlo (MCMC) method. The advantage of a MCMC method here is the directness from the fit result Jacobian, meaning directly from the fit information we can sample the distribution of the parameters. Of course, we have made the assumption that the Hessian of the cost-function is Gaussian, but this further allows us to simply use a multivariate normal sampler of the covariance matrix as the MCMC distribution.

Given N samples with the covariant MCMC sampler, we can take the 95th percentile credible interval on any predicted point by the fit function. I have made plots both for the 95% credible interval over distance and energy, seen in fig 3.5.

The fit results with the errors are quite reasonable, and the confidence region remains close to the function, straying only significantly in the areas without much data, as below 500keV and above 2500keV. The shapes have some sense in this regard as well as the exponential dropoff in distance, confirming our results are reasonable. For confirmation of the fit, I graph the modeled yields for each point and compare to the data in figure 3.6.

One concern with the efficiency fit, however, is the lack of data at or below the 440keV mark, which is needed for the $^{12}C+^{12}C$ experiment. This is significant because we should expect to see some drop-off of the efficiency in the detector as we get to the lowest energies (less than 200keV), which is not modeled within our current data and fit. To address this, we have compared the fit with simulations not presented in this work, and confirm the trend of the efficiency for the purpose of this thesis.

3.2 Carbon on Carbon Measurements

In June and July of 2025, runs were carried out using a $^{12}C^{2+}$ beam on “infinite” Carbon targets using the 3.5 MV Singletron accelerator at the Bellotti IBF. The runs were labelled between 450 and 600, and the targets used were labelled ZXF0.8, ZXF0.95, and ZXF1.03. The full list of each run analyzed with yield information can be found in table 3.4.

In February and March of 2026, additional lower energy runs were carried out with a target labelled ZXF1.01, over runs labelled 790-810. Figure 3.7 shows the resulting spectrum of a run (802) at 2.965 MeV E_{cm}, from which the peaks have been identified in table 3.5.

The 440 keV and 1640 keV proton and alpha channel lines, respectively can be found easily, along with many background peaks. The Hydrogen BiB peaks of 2420 keV for ^{1}H and 3100 keV for ^{2}H (see section 2.3), are very prominent, and other BiB including detector activation Ge peaks can be found as well. Curiously, we see a very large peak at 197 keV in most runs, which we have identified as a beam-induced ^{19}F excitation which may be present in the target or glue, but remain uncertain about.

3.2.1 Spectral Analysis

The 1640 keV and 440 keV peaks respectively can be seen in figure 3.8. Visible next to the 440 keV peak is the 511 keV annihilation peak, which is much taller and less broad than the 440 keV peak. The 511keV annihilation peak is produced in many ways, namely from background β^+ decay or the rare ^{24}Mg fusion product. This represents the physical environment well, since the beam-influenced peak is broadened due to the Doppler effect (see sec. 2.6) as well as less intense than the 511 keV peak due to the prevalence of annihilation photons.

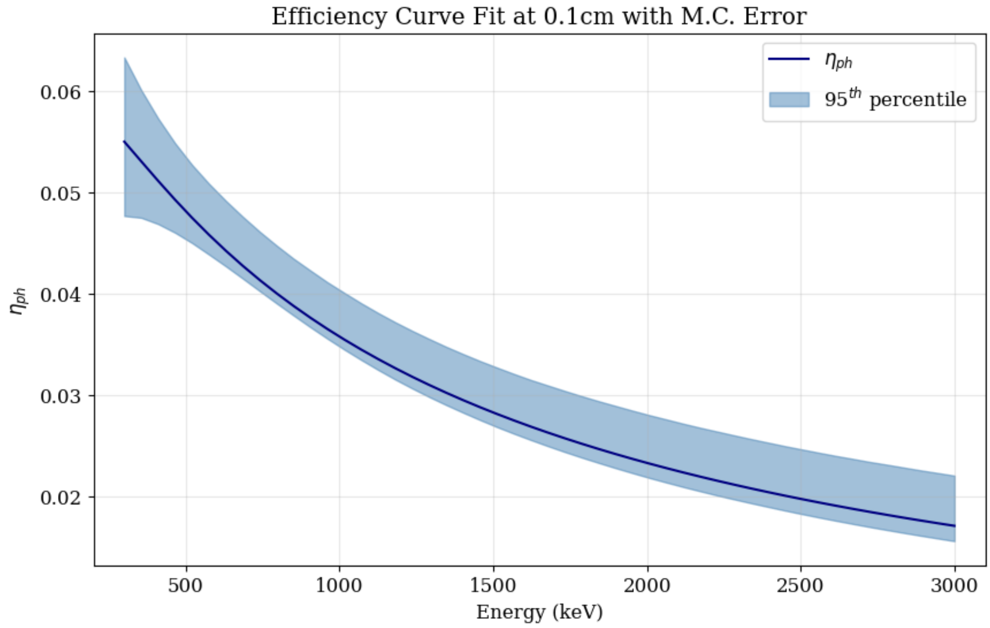

(A) Photopeak efficiency values over energy ranges at 1cm detector distance

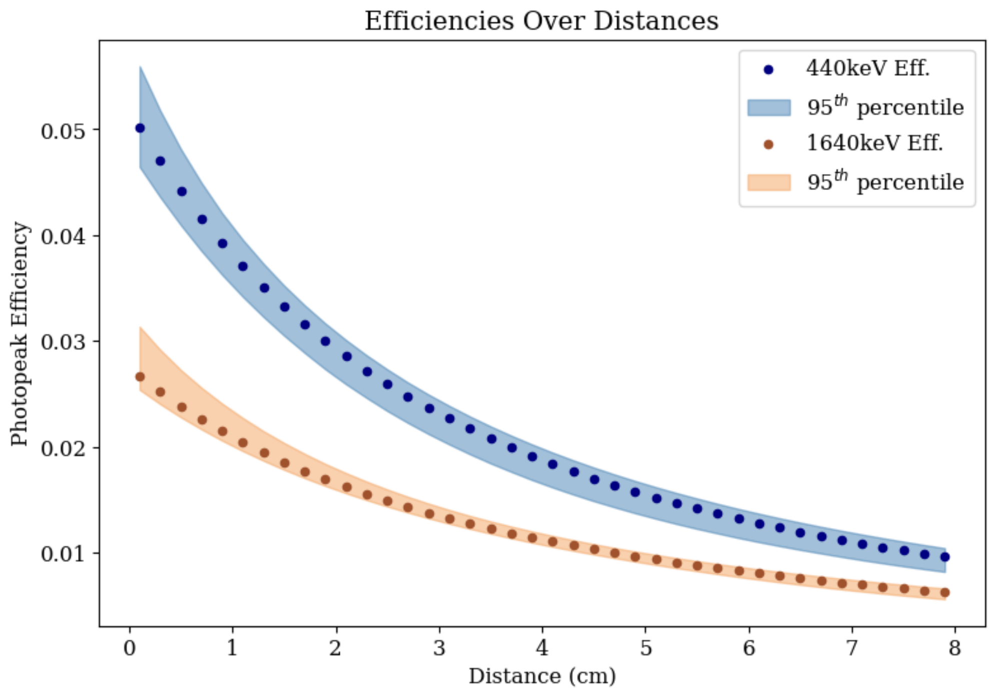

(B) Photopeak efficiency values over detector distances at both 440keV and 1640keV energies

FIGURE 3.5: photopeak efficiencies from function fitted to best values with MCMC 95th percentile confidence region

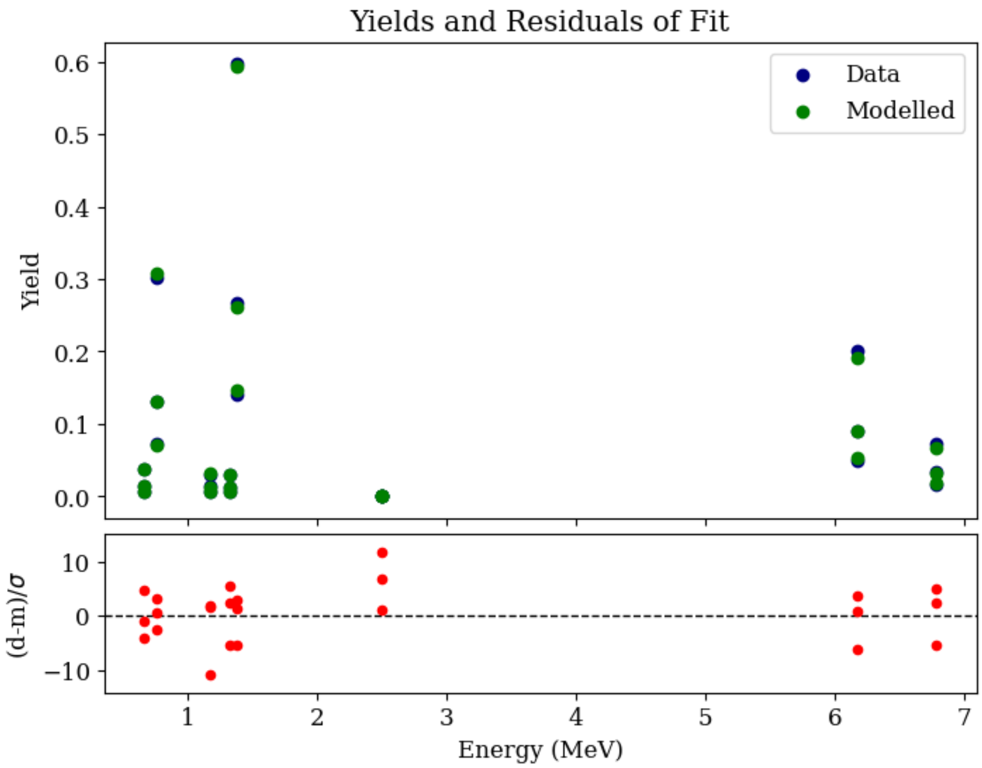

FIGURE 3.6: Yields of Efficiency data compared to model's yield values. Residuals on bottom graph scaled by the standard deviation.

Run	Length (s)	Energy (MeV)	Target	Deposited Charge (C)
498	4397	3.149	ZXF0.8	0.39230
505	6022	3.089	ZXF0.8	0.51216
506	5610	3.069	ZXF0.8	0.46971
511	9282	3.008	ZXF0.8	0.52800
563	24900	2.362	ZXF1.03	0.24848
569	780	3.371	ZXF0.95	0.07834
570	19860	2.564	ZXF0.95	1.65921
571	3300	2.564	ZXF0.95	0.34955
577	24900	2.362	ZXF1.03	2.42770
581	32820	2.220	ZXF1.03	2.16177
587	19920	2.039	ZXF1.03	1.43412
589	11580	2.474	ZXF1.03	0.92266
793	12240	2.599	ZXF1.01	0.35907
794	3300	2.867	ZXF1.01	0.20772
799	43500	2.503	ZXF1.01	2.18678
800	17880	2.640	ZXF1.01	0.52477
802	5040	2.965	ZXF1.01	0.34101
805	32192	2.451	ZXF1.01	2.13998

TABLE 3.4: Table of run data for C12-C12 experiment

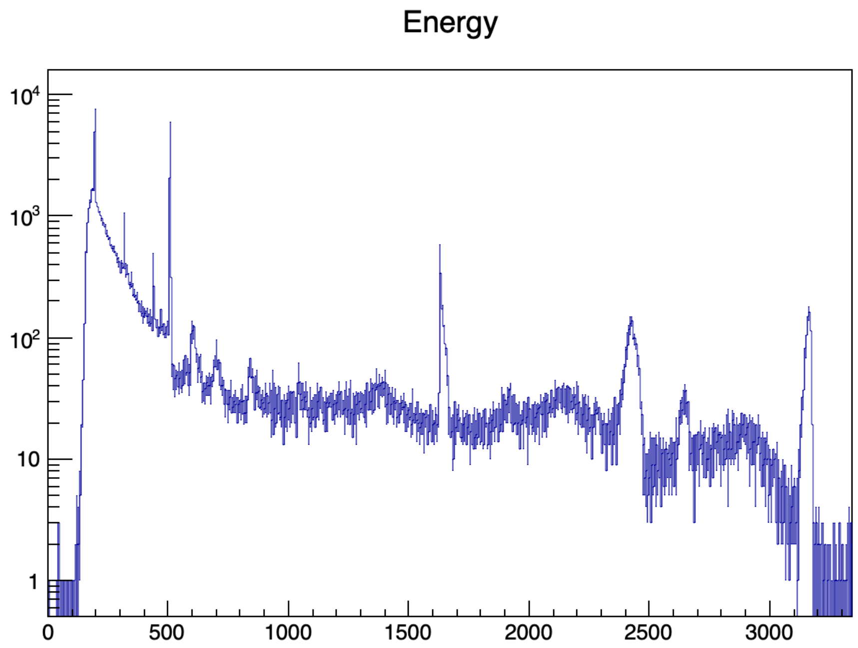

FIGURE 3.7: Spectrum of 12C at 2.965 MeV in Center of Mass, x-axis in energy binned at 1keV per bin

E (keV)	Peak	E (keV)	Peak
197	^{19}F?	847	^{27}Al
320	^{21}Ne	872	^{23,24}Na
440	^{23}Na	1050	^{23}Na
470	^{24}Na	1640	^{20}Ne
511	Annh.	2420	^{1}H BiB, ^{23}Na
600	^{74,72}Ge	2640	^{23}Na
630	^{23}Na	3100	^{2}H BiB
700	^{72}Ge		

TABLE 3.5: Identified peaks of the 2.965 MeV E_{cm} ^{12}C run

This broadening is also well seen in the stronger 1640keV region, where intense broadening creates a very broad peak, with peculiar shape. To better understand that shape, we can look at the peak in linear scaling as well as a higher energy run with higher counts in figure 3.9. In this figure it is evident the same structure that is seen in figure 2.11 with a peak at E_0 and a Doppler broadened curve.

Additionally, we can see that the Doppler peak moves further from the E_0 peak as the E_{CM} increases. This also makes sense as the proportion of non-zero velocity particles increases as the velocity increases due to longer slowing down times. Further, there are very little Doppler-decreased counts (below E_0), which follows due to the kinematics favoring forward-scattering of the decay particle, along with the 0° angle of the detector.

The lowest energy runs have severely reduced count rates, as seen in figure 3.10 which shows a spectrum of run 587 with $E_{\mathrm{CM}} = 2.040$ MeV. The difference in count rate is extreme, with the 440 keV region in the lower energy plot being completely dominated

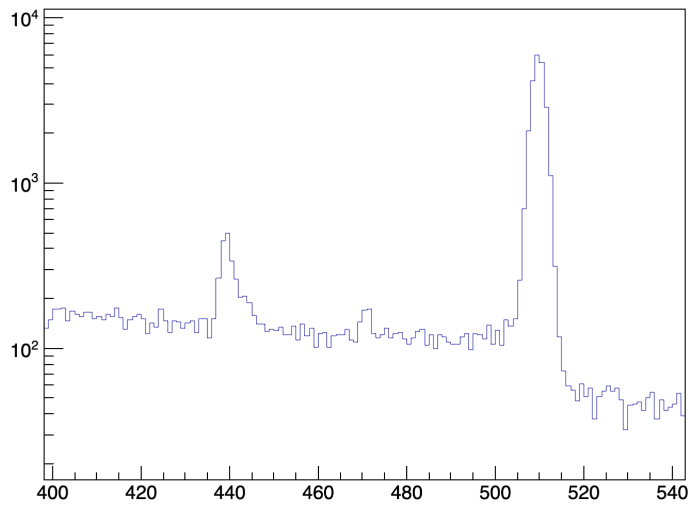

(A) 440 keV peak, also visible on right is the 511 keV annihilation peak

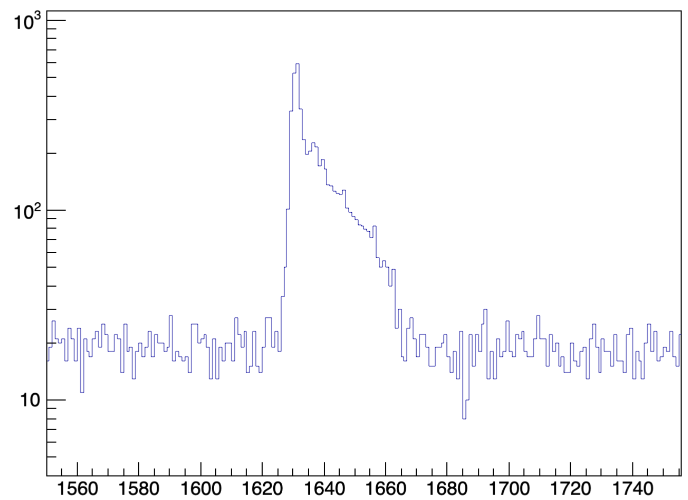

(B) 1640 keV peak

FIGURE 3.8: Close-ups of peaks of run 802 at 2.965 MeV E_{CM} in logarithmic scale. Energy binned at 1keV per bin

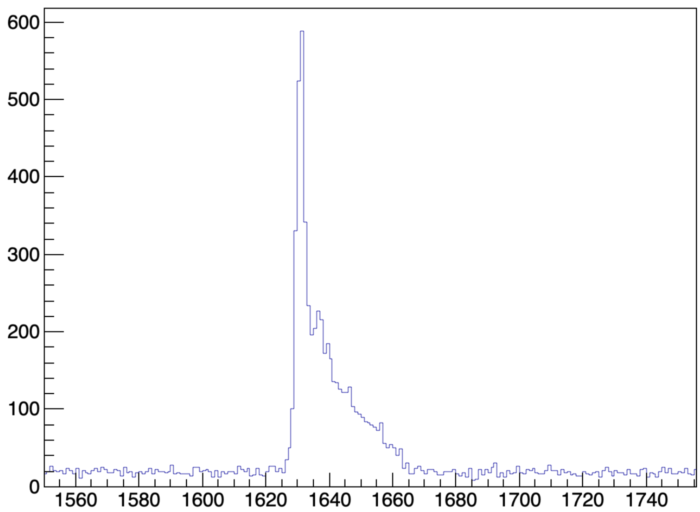

(A) Run 802 at 2.965 MeV E_{CM}

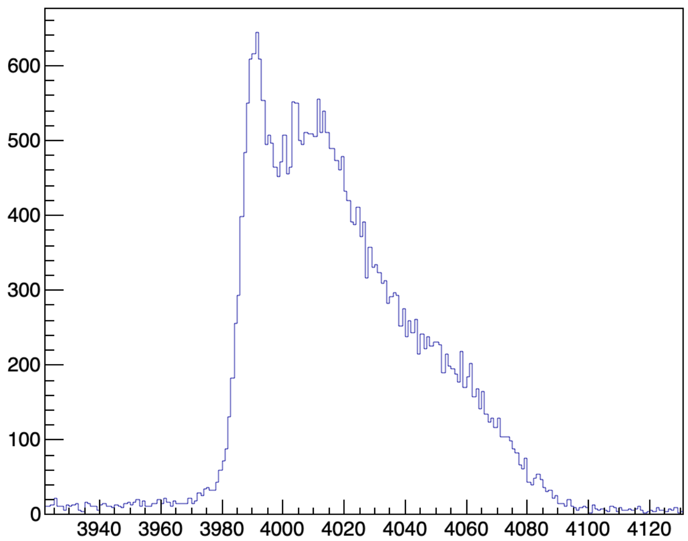

(B) Run 569 at 3.371 MeV E_{CM}, note x-axis not Energy-corrected

FIGURE 3.9: Linear scale of 1640 keV peak in 2.965 MeV E_{CM} and 3.371 MeV E_{CM}

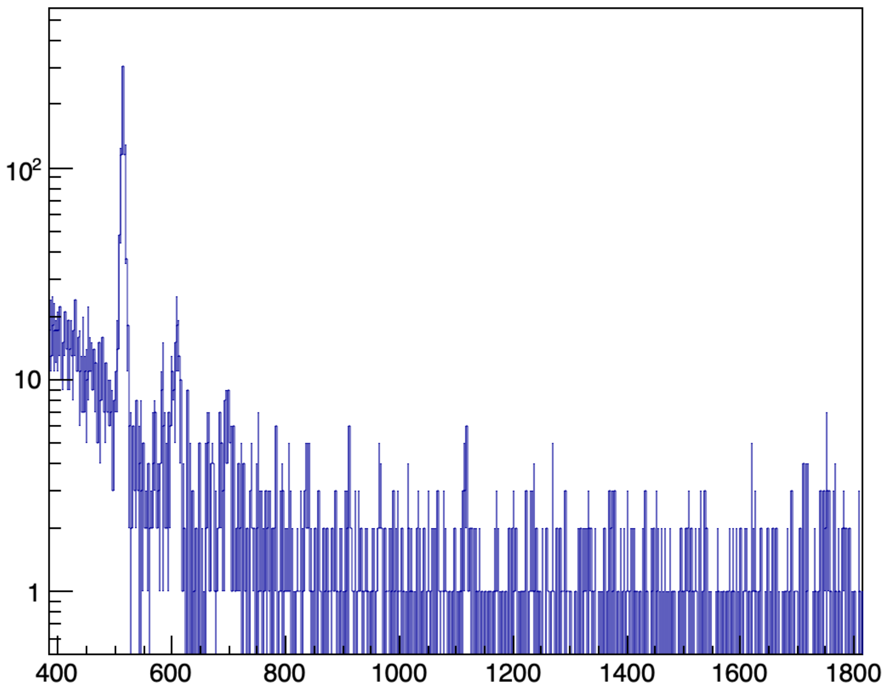

FIGURE 3.10: Spectrum of run 587 at 2.040 MeV E_{CM} in logarithmic scale. Visible is the 511 keV annihilation line

by noise, meaning we can only assign a statistical upper limit to this value. Other runs at similarly low energies have the same problem, with very high error dominating the result.

3.2.2 Calculating Yields

To measure the count rate in a region, I use the same method as section 3.1.2, in taking and average of a region of background bins above and below the region of interest (ROI), and subtracting from the total counts [16]. I calculate the error on the count rate as well the same using equation 3.8. A visualization of this method can be seen in figure 3.11, where the black box shows the region being subtracted from the peak integration as the background.

This specific example is a simple region to judge due to the high count rate. Lower energy E_{CM} peaks are much harder to judge the ROI, due to dominance of the background. Thus, there is some small systematic error in counting these peaks as judgement must be made. We avoid fitting the peak with a gaussian fit due to the non-gaussian nature of the peaks, which may add large uncertainty to our peak integration. For the lowest peaks (such as seen in figure 3.10), where there may be no indication of a peak, a ROI is selected based on the appropriate closest run in E_{CM} and target.

In the case where a peak is uncertain, we must compare the counts to a critical limit to determine if we can say the peak is statistically significant. If not, we replace the integrated counts number with a statistical upper limit [16]. First, to calculate the

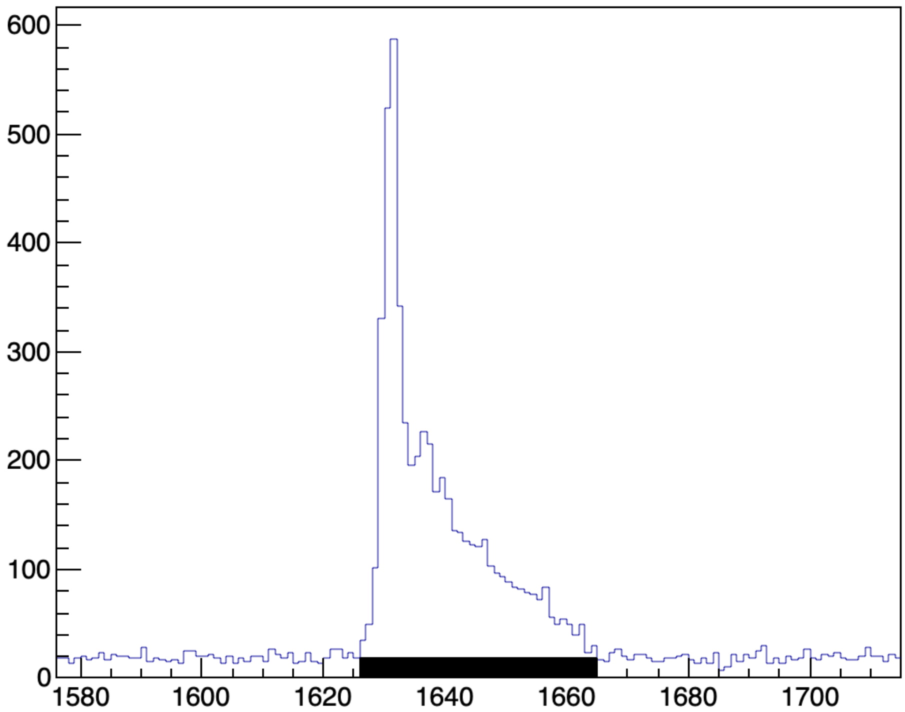

FIGURE 3.11: Spectrum of run 802 in linear scale showing the 1640keV ROI. The black region indicates the region of background being subtracted from the peak

critical limit, we must choose a level of significance, which I choose the 95% level or $\alpha = 0.05$. Then we use the following equation to calculate the critical limit:

$$L_C = 1.645\sqrt{B\left(1 + \frac{n}{2m}\right)} \tag{3.9}$$

with B as the estimate number of background counts beneath the peak, n as the number of bins in the peak integration, and m as the number of bins on either side of the peak used as background estimate (as in equation 3.8). This is obvious as the 95% limit would be $L_C = 1.645\sigma_0$ with σ_0 as the standard deviation of the background estimate, which we approximate as $\sqrt{B(1 + \frac{n}{2m})}$.

Given a non-significant peak detection, we calculate the upper limit with the following:

$$L_U = A + 1.645\sqrt{A + B\left(1 + \frac{n}{2m}\right)} \tag{3.10}$$

with B, n, m as before and A as the integrated peak area (with background subtracted). This allows us when we cannot estimate reasonably how many counts are in the peak to estimate what the minimum number of counts we would need to reach statistical significance. As in this case we have no statistical significance, we can say it is definitely below that amount, giving an upper limit. Note that $L_U = L_C$ in the event that $A = 0$, thus if the integrated counts is 0 (or negative), we can take the critical limit as the upper limit.

For run 587's 440 keV region, we have this case with $B = 133.38$, $n = 25$, $m = 50$, giving $L_C = 21.32$ counts, compared to an integrated peak area of -18 counts, so we assign $L_U = 21.32$. The background subtraction method can be visualized in figure 3.12a, where it is obvious there is no peak. The boundaries are chosen from the peak of run 577, which is 2.362 MeV compared to run 587 at 2.039 MeV, which has its peak and background plotted in figure 3.12b.

We next take the number of incident particles as the charge deposited on the target divided by $2e$ where e is the elementary charge of an electron. The factor of 2 is needed due to the beam being a $^{12}C^{2+}$ beam, meaning it deposits $2e$ for every atom of carbon incident.

With this, and with the efficiency given by the fit from section 3.1.2, we can use equation 2.1 with the relation $N_{\text{reactions}} = \frac{N_\gamma}{\eta(E)}$ to calculate preliminary infinite yields for the data. The results of this calculation is given in table 3.6, and is plotted in figure 3.13.

Run	Energy (MeV)	Target	440keV Yield	1640keV Yield
498	3.149	ZXF0.8	1.40×10^{-13}	1.06×10^{-12}
505	3.089	ZXF0.8	4.89×10^{-13}	7.43×10^{-14}
506	3.069	ZXF0.8	1.40×10^{-13}	1.06×10^{-12}
511	3.008	ZXF0.8	3.66×10^{-14}	2.08×10^{-13}
563	2.362	ZXF1.03	1.39×10^{-14}	5.46×10^{-14}
569	3.371	ZXF0.95	8.44×10^{-13}	4.69×10^{-12}
570	2.564	ZXF0.95	5.02×10^{-15}	4.53×10^{-15}
571	2.564	ZXF0.95	3.59×10^{-15}	1.41×10^{-14}
577	2.362	ZXF1.03	2.37×10^{-16}	4.37×10^{-16}
581	2.220	ZXF1.03	4.77×10^{-16}	3.11×10^{-16}
587	2.039	ZXF1.03	8.93×10^{-17}*	7.92×10^{-17}
589	2.474	ZXF1.03	2.52×10^{-16}	6.24×10^{-16}
793	2.599	ZXF1.01	2.31×10^{-15}	1.07×10^{-14}
794	2.867	ZXF1.01	1.57×10^{-14}	7.97×10^{-14}
799	2.503	ZXF1.01	7.98×10^{-16}	1.30×10^{-15}
800	2.640	ZXF1.01	1.76×10^{-15}	2.65×10^{-14}
802	2.965	ZXF1.01	2.74×10^{-14}	1.64×10^{-13}
805	2.451	ZXF1.01	2.35×10^{-16}	3.35×10^{-16}

TABLE 3.6: Table C12-C12 Yields for both 440 keV and 1640 keV regions. * represents statistical upper limit

To get the statistical errors on the yield values, I must combine all sources of error. The first being the integration error, mentioned above, and the second being the error on the efficiency model estimate, as described in section 3.1.3. Not included is the error on the charge integration by the faraday cup which is instead treated as a systematic error in section 3.4.

$$\sigma_Y = Y \cdot \sqrt{\left(\frac{\sigma_\gamma}{N_\gamma}\right)^2 + \left(\frac{\sigma_\eta}{\eta}\right)^2} \tag{3.11}$$

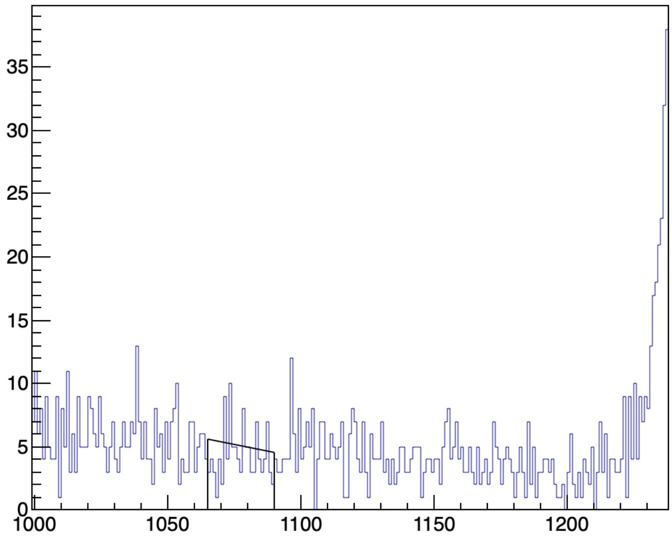

(A) Spectrum of run 587 at 2.039 MeV E_{CM}. Note that there is no evident peak, but the 511 keV peak can be seen on the right edge.

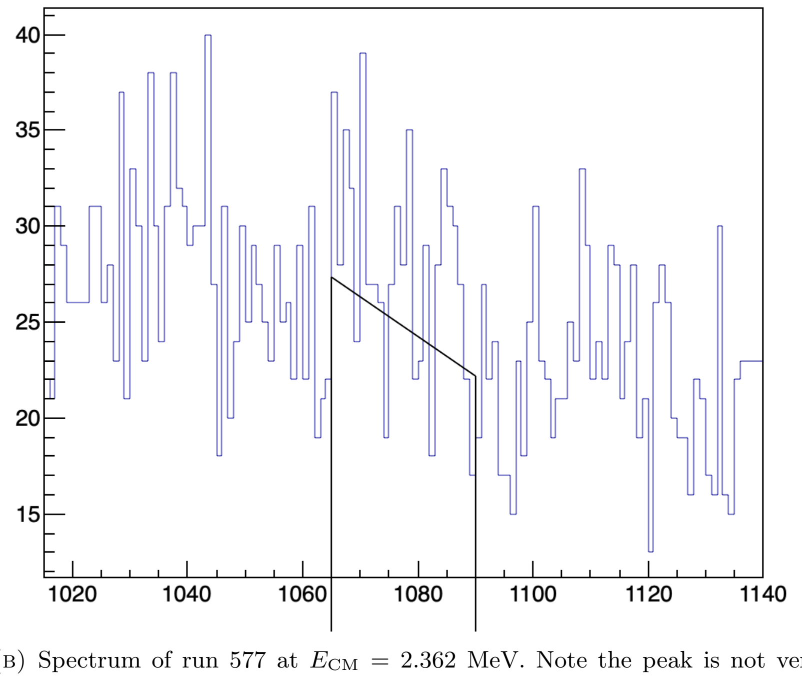

(B) Spectrum of run 577 at $E_{\mathrm{CM}} = 2.362$ MeV. Note the peak is not very visible to the naked eye, but the background box is mostly below the counts

FIGURE 3.12: Spectra of low-count peaks in linear scale.

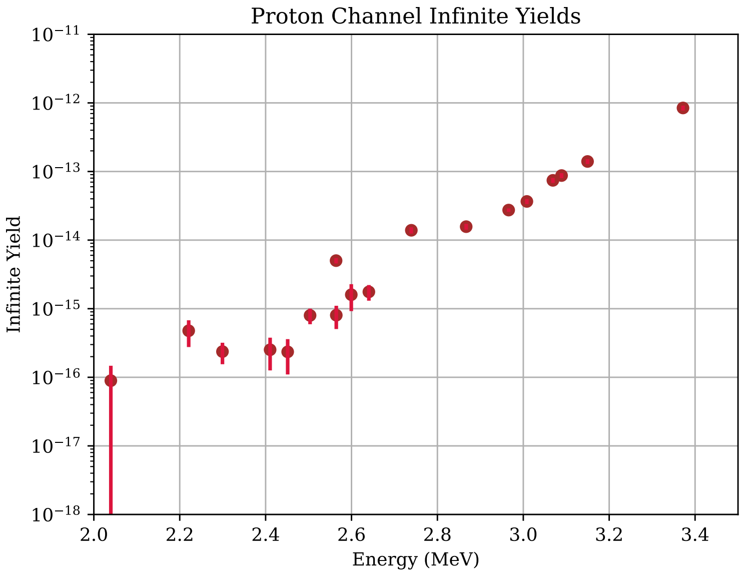

(A) 440 keV Proton channel emission yields

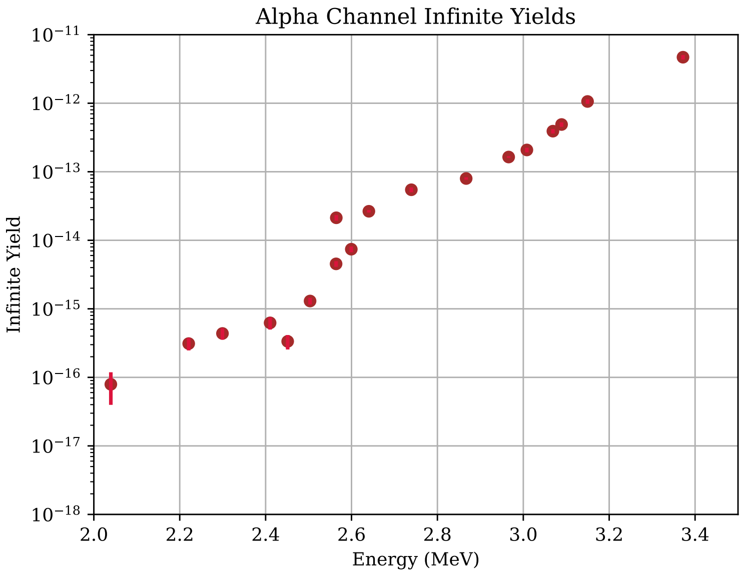

(B) 1640 keV Alpha channel emission yields

FIGURE 3.13: Preliminary infinite yields of LUNA data taken in 2025 and 2026 over 2.039 MeV to 3.4 MeV

where $\frac{\sigma_\gamma}{N_\gamma}$ is the ratio of the peak integration error to the integrated counts and $\frac{\sigma_\eta}{\eta}$ is the ratio of the efficiency model error and the model value.

3.3 Comparison With Previous Literature

To compare our preliminary yield values to both Spillane et al. [5] and Tumino et al. [6], we gather their data for the modified astrophysical factor $\tilde{S}(E)$ given in units of barns*MeV. Rather than calculate the astrophysical factor ourselves to compare we can calculate an infinite yield from their data. The advantage of doing it this way around is that we need much fewer data points, as with the infinite yield we must take two points to calculate each $\Delta Y^\infty(E_{eff})$ in equation 2.6.

Using equation 2.4, we can calculate each infinite yield given the cross section and stopping power. To get the cross section, we can use equation 1.4 to get:

$$Y^\infty(E_0) = \int_0^{E_0} \frac{\tilde{S}(E)}{\epsilon(E)E} e^{-2\pi\eta - gE} dE \tag{3.12}$$

This equation requires the calculation of many values, which I perform in excel. Most importantly, we need the stopping power of the carbon atoms in the target. Calculated in SRIM (Stopping and Range of Ions in Matter) [21] using a data-interpolation model, we obtain stopping powers from 10 keV to 10000 keV at varying steps in eV/(10^{15}atoms/cm^2). The stopping power calculation in SRIM represents a large source of systematic error, which is not fully modeled within this thesis. Converting to the center-of-mass frame, and MeV/(atoms/cm^2), I obtain a usable range of stopping powers for the integration, except that the points do not align with the $\tilde{S}(E)$ data.

Thus I built an interpolating function for the stopping powers in excel as (with example columns):

```
=INDEX($AD$2:$AD$78, MATCH(AG3, $AB$2:$AB$78, 1)) +
(AG3 - INDEX($AB$2:$AB$78, MATCH(AG3, $AB$2:$AB$78, 1))) *
(INDEX($AD$2:$AD$78, MATCH(AG3, $AB$2:$AB$78, 1)+1) -
INDEX($AD$2:$AD$78, MATCH(AG3, $AB$2:$AB$78, 1))) /
(INDEX($AB$2:$AB$78, MATCH(AG3, $AB$2:$AB$78, 1)+1) -
INDEX($AB$2:$AB$78, MATCH(AG3, $AB$2:$AB$78, 1)))
```

where column AB is the stopping power energies (in MeV), column AD is the stopping power values, and column AG is the energy of the point to interpolate (in MeV) – this example for cell AG3. This interpolator is very simple in that it approximates the space between each point as a linear function and estimates the value based on the distance to each point.

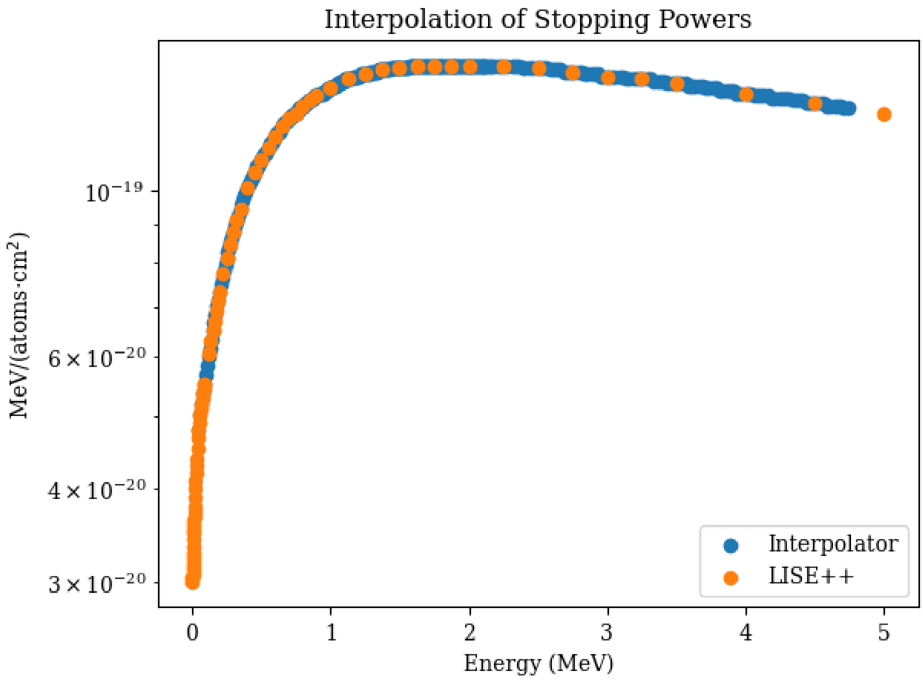

FIGURE 3.14: Comparison of stopping powers from SRIM and excel interpolation function to Spillane et al. [5] $\tilde{S}(E)$ data energy steps

While simple, this interpolator works well for our purposes, and the result is compared with the SRIM data in figure 3.14. This shows very reasonable approximations, and will be used for the integration.

Then I calculate the $-2\pi\eta - gE$ factor for each energy, and then use the `SUMPRODUCT` function in excel to create the integration over each datapoint. With each yield being integrated over all previous points of the $\tilde{S}(E)$ and stopping power, we can compare the Spillane et al. [5] and Tumino et al. [6] data for both the proton and alpha channels with our preliminary yields. This result can be seen in figure 3.15.

3.4 Results and Discussion

The results are promising in that they follow previous results within reason. It appears as though our preliminary results follow the higher yield curve of Tumino et al. [6]'s work rather than Spillane et al. [5].

It is important to note the strong presence of systematic error, however, which is especially notable at the two 2.564 MeV points. With two separate runs, the yields calculated exclude each other outside of their errors. This signals that there is significant systematic error within the results. An estimate of the sources of systematic error can be seen in table 3.7, and the total is the sum in quadrature.

The 2.6–2.8 MeV region deviates noticeably from the otherwise good agreement with Spillane et al. seen at higher energies. This may be due to beam-induced background

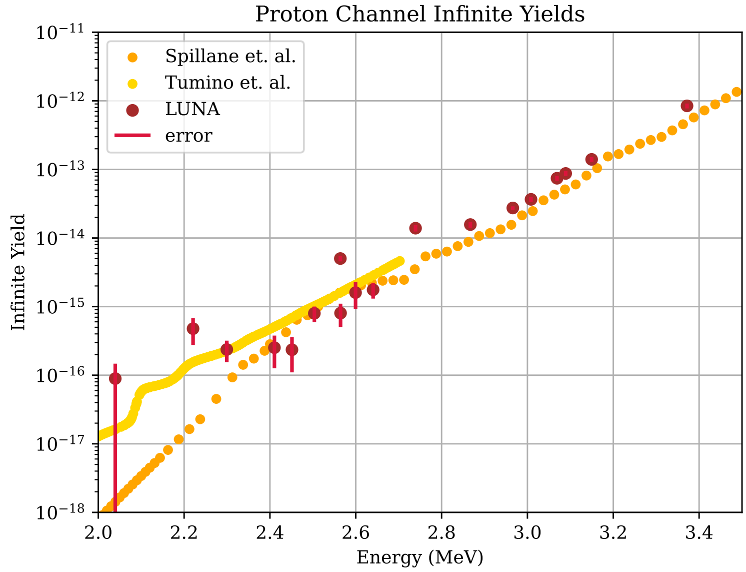

(A) 440 keV Proton channel emission yields

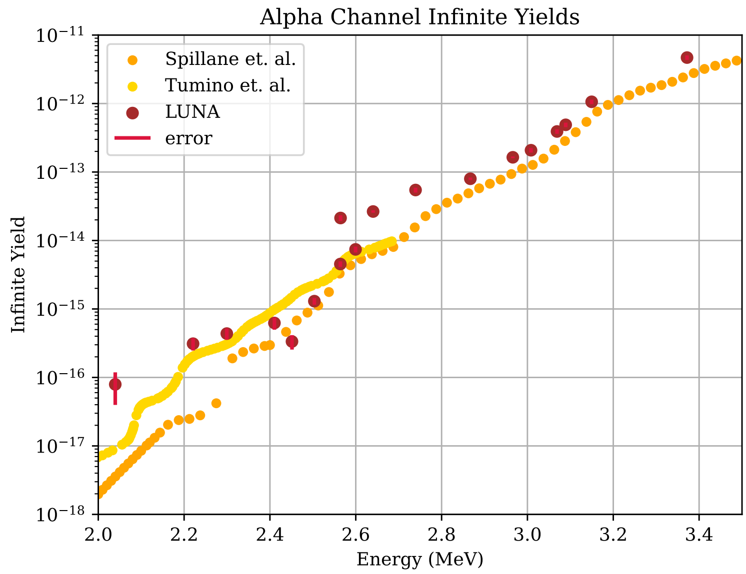

(B) 1640 keV Alpha channel emission yields

FIGURE 3.15: Comparison of LUNA preliminary infinite yields with Spillane et al. [5] and Tumino et al. [6] including error bars

Source	Error Estimate
Current Reading	1.5%
Beam Energy	1.5%
Stopping Powers	4%
Efficiency Calibration	5%
Total	6.7%

TABLE 3.7: Systematic Error Estimates for LUNA $^{12}C+^{12}C$ Experiment

effects, possibly from backscattering of ^{12}C on ^{1}H or ^{2}H (also the reverse is possible). To determine this effect, further study is needed and is out of the scope of this work.

In the lower energy regions, where the data appears to follow the trend of Tumino et al. [6], the data is too sparse to draw direct conclusions. Further beam time is needed in this area to clarify the resonance structure and confirm the trend. Additionally, GEANT4 simulations of the experiment should be done to conduct peak shape analysis and avoid counting BiB in our peaks.

Thus, while it appears that the low energy results follow the results of Tumino et al. [6] more closely, it should be taken as a first step analysis of the experiment. The next steps are underway at LUNA as simulations are in development with additional data, and will further the analysis done in this thesis.

Bibliography

[1] Dr. Christian Iliadis. *Nuclear Physics of Stars.* Wiley-VCH, 2007.

[2] Alessandro Chieffi et al. The status of ^{12}C+^{12}C fusion process. *Eur. Phys. J. A*, 61(12):280, 2025. doi: 10.1140/epja/s10050-025-01759-3.

[3] Timothy Spillane. *Study of the fusion reaction ^{12}C+^{12}C towards the Gamow energy.* PhD thesis, University of Conneticut, 2008.

[4] E. Almqvist, D. A. Bromley, and J. A. Kuehner. Resonances in ^{12}C on carbon reactions. *Phys. Rev. Lett.*, 4:515–517, May 1960. doi: 10.1103/PhysRevLett.4.515. URL https://link.aps.org/doi/10.1103/PhysRevLett.4.515.

[5] T. Spillane, F. Raiola, C. Rolfs, D. Schürmann, F. Strieder, S. Zeng, H.-W. Becker, C. Bordeanu, L. Gialanella, M. Romano, and J. Schweitzer. Fusion reactions near the gamow energy. *Physical Review Letters*, 98(12), March 2007. ISSN 1079-7114. doi: 10.1103/physrevlett.98.122501. URL http://dx.doi.org/10.1103/PhysRevLett.98.122501.

[6] A. Tumino, C. Spitaleri, M. La Cognata, S. Cherubini, G. L. Guardo, M. Gulino, S. Hayakawa, I. Indelicato, L. Lamia, H. Petrascu, R. G. Pizzone, S. M. R. Puglia, G. G. Rapisarda, S. Romano, M. L. Sergi, R. Spartá, and L. Trache. An increase in the 12C + 12C fusion rate from resonances at astrophysical energies. *Nature.*, 557:687–690, May 2018.

[7] Monpribat, E., Martinet, S., Courtin, S., Heine, M., Ekström, S., Jenkins, D. G., Choplin, A., Adsley, P., Curien, D., Moukaddam, M., Nippert, J., Tsiatsiou, S., and Meynet, G. A new 12C + 12C nuclear reaction rate: Impact on stellar evolution. *A&A*, 660:A47, 2022. doi: 10.1051/0004-6361/202141858. URL https://doi.org/10.1051/0004-6361/202141858.

[8] W. P. Tan, A. Boeltzig, C. Dulal, R. J. deBoer, B. Frentz, S. Henderson, K. B. Howard, R. Kelmar, J. J. Kolata, J. Long, K. T. Macon, S. Moylan, G. F. Peaslee, M. Renaud, C. Seymour, G. Seymour, B. Vande Kolk, M. Wiescher, E. F. Aguilera, P. Amador-Valenzuela, D. Lizcano, and E. Martinez-Quiroz. New measurement of ^{12}C+^{12}C fusion reaction at astrophysical energies. *Phys. Rev. Lett.*, 124:192702, May 2020. doi: 10.1103/PhysRevLett.124.192702. URL https://link.aps.org/doi/10.1103/PhysRevLett.124.192702.

[9] John R. Patterson, Heiner Winkler, and Clyde S. Zaidins. Experimental investigation of the stellar nuclear reaction ^{12}C + ^{12}C at low energies. *The Astrophysical Journal*, 157:367, 1969. URL https://api.semanticscholar.org/CorpusID:120500961.

[10] Laboratory for underground nuclear astrophysics, 2026. URL https://luna.lngs.infn.it/index.php.

[11] R M Gesuè, S Turkat, J Skowronski, M Aliotta, L Barbieri, F Barile, D Bemmerer, A Best, A Boeltzig, C Broggini, C G Bruno, A Caciolli, M Campostrini, F Casaburo, F Cavanna, T Chillery, G F Ciani, P Colombetti, A Compagnucci, P Corvisiero, L Csedreki, T Davinson, D Dell'Aquila, R Depalo, A Di Leva, Z Elekes, F Ferraro, A Formicola, Zs Fülöp, G Gervino, G Gosta, A Guglielmetti, C Gustavino, Gy Gyürky, G Imbriani, M Junker, M Lugaro, P Marigo, J Marsh, E Masha, R Menegazzo, D Mercogliano, V Paticchio, D Piatti, P Prati, D Rapagnani, V Rigato, D Robb, L Russell, R S Sidhu, B Spadavecchia, O Straniero, T Szücs, S Zavatarelli, and (LUNA collaboration). Detector characterization for a new 12C+12C reaction study at luna. *Journal of Physics G: Nuclear and Particle Physics*, 52(10):105103, oct 2025. doi: 10.1088/1361-6471/ade0dc. URL https://doi.org/10.1088/1361-6471/ade0dc.

[12] A. Compagnucci, A. Formicola, M. Campostrini, J. Cruz, M. Aliotta, C. Ananna, L. Barbieri, F. Barile, D. Bemmerer, A. Best, A. Boeltzig, C. Broggini, C. G. Bruno, A. Caciolli, F. Casaburo, F. Cavanna, G. F. Ciani, P. Colombetti, P. Corvisiero, L. Csedreki, T. Davinson, R. Depalo, A. Di Leva, Z. Elekes, F. Ferraro, Zs. Fülöp, A. Guglielmetti, C. Gustavino, Gy. Gyürky, G. Imbriani, M. Junker, M. Lugaro, P. Marigo, J. Marsh, E. Masha, R. Menegazzo, V. Paticchio, D. Piatti, P. Prati, D. Rapagnani, V. Rigato, D. Robb, L. Schiavulli, R. S. Sidhu, J. Skowronski, O. Straniero, T. Szücs, S. Turkat, and S. Zavatarelli. Towards a comprehensive study of the ^{14}N(p,γ)^{15}O astrophysical key reaction: Description of the experimental technique including novel target preparation. *The European Physical Journal A*, 61(8):191, 2025. doi: 10.1140/epja/s10050-025-01658-7. URL https://doi.org/10.1140/epja/s10050-025-01658-7.

[13] A. Sen, G. Domínguez-Cañizares, N.C. Podaru, D.J.W. Mous, M. Junker, G. Imbriani, and V. Rigato. A high intensity, high stability 3.5 MV Singletron™ accelerator. *Nuclear Instruments and Methods in Physics Research Section B: Beam Interactions with Materials and Atoms*, 450:390–395, 2019. ISSN 0168-583X. doi: https://doi.org/10.1016/j.nimb.2018.09.016. The 23rd International Conference on Ion Beam Analysis.

[14] Annika Willer. Study of the ^{12}C+^{12}C reactions for astrophysics. Master's thesis, Technische Universität Dresden, 2025.

[15] Hermann Kolanoski and Norbert Wermes. *Particle Detectors Fundamentals and Applications*. Oxford University Press, 2020.

[16] Gordon R. Gilmore. *Practical Gamma-ray Spectrometry*. John Wiley & Sons, Ltd, 2nd edition, 2008.

[17] Jakub Skowronski. *Complete Study of Proton Capture on Carbon Isotopes at Astrophysical Energies*. PhD thesis, Università Degli Studi di Padova, 2023.

[18] National nuclear data center, 2026. URL https://www.nndc.bnl.gov.

[19] Z. Kis, B. Fazekas, J. Östör, Zs. Révay, T. Belgya, G.L. Molnár, and L. Koltay. Comparison of efficiency functions for Ge gamma-ray detectors in a wide energy range. *Nuclear Instruments and Methods in Physics Research Section A: Accelerators, Spectrometers, Detectors and Associated Equipment*, 418(2):374–386, 1998.

[20] scipy.optimize.least_squares. URL https://docs.scipy.org/doc/scipy/reference/generated/scipy.optimize.least_squares.html.

[21] James F. Ziegler. Interactions of ions with matter. URL http://www.srim.org.